




# Multiwavelength Modeling of the SED of Nova V339 Del: Stopping the Wind and Long-lasting Super-Eddington Luminosity with Dust Emission

Augustin Skopal 

Astronomical Institute, Slovak Academy of Sciences, 059 60 Tatranská Lomnica, The Slovak Republic; [skopal@ta3.sk](mailto:skopal@ta3.sk)

Received 2018 July 24; revised 2019 April 17; accepted 2019 May 1; published 2019 June 11

## Abstract

During the classical nova outburst, the radiation generated by the nuclear burning of hydrogen in the surface layer of a white dwarf (WD) is reprocessed by the outer material into different forms at softer energies, whose distribution in the spectrum depends on the nova age. Using the method of multiwavelength modeling the spectral energy distribution (SED), we determined physical parameters of the stellar, nebular, and dust component of radiation isolated from the spectrum of the classical nova V339 Del from day 35 to day 636 after its explosion. The transition from the iron-curtain phase to the supersoft source phase (days 35–72), when the optical brightness dropped by 3–4 mag, the absorbing column density fell by its circumstellar component from  $\sim 1 \times 10^{23}$  to  $\sim 1 \times 10^{21} \text{ cm}^{-2}$ , and the emission measure decreased from  $\sim 2 \times 10^{62}$  to  $\sim 8.5 \times 10^{60} \text{ cm}^{-3}$ , was caused by stopping down the mass loss from the WD. The day 35 model SED indicated an oblate shape of the WD pseudophotosphere and the presence of the dust located in a slow equatorially concentrated outflow. The dust emission peaked around day 59. Its coexistence with the strong supersoft X-ray source in the day 100 model SED constrained the presence of the disk-like outflow, where the dust can spend a long time. Both the SED models revealed a super-Eddington luminosity of the burning WD at a level of  $(1\text{--}2) \times 10^{39} (d/4.5 \text{ kpc})^2 \text{ erg s}^{-1}$ , lasting from  $\sim$ day 2 to at least day 100.

**Key words:** novae, cataclysmic variables – stars: fundamental parameters

## 1. Introduction

The nova phenomenon results from a thermonuclear runaway (TNR) on the surface of a white dwarf (WD) accreting hydrogen-rich material from its companion in a binary system (e.g., Bode & Evans 2008; Starrfield et al. 2016, for a review). The TNR event significantly increases the luminosity and ejects material of  $10^{-3}$  to  $10^{-7} M_{\odot}$  at velocities  $\gtrsim 10^3 \text{ km s}^{-1}$  (e.g., Gallagher & Starrfield 1978; Kato & Hachisu 1994). The energy released near the WD surface is thus reprocessed through the outer material, giving rise to the spectral energy distribution (SED) that changes across the electromagnetic spectrum with the nova age. In this work we introduce modeling the SED of a classical nova V339 Del at critical dates of its evolution to obtain new information about the nova explosion.

Classical nova V339 Del (Nova Delphini 2013 = PNV J20233073+2046041) was discovered by Koichi Itagaki on 2013 August 14.584 UT at a visual magnitude of  $\sim 6.8$  (Nakano 2013). Its progenitor was identified by Denisenko et al. (2013) as the blue star USNO-B1.0 1107-0509795 ( $B \sim 17.2\text{--}17.4$ ,  $R \sim 17.4\text{--}17.7$ ). Munari & Henden (2013) found the progenitor also on the Asiago 1979–82 plates and within observations taken by the APASS survey<sup>1</sup> in 2012 April, whereas Deacon et al. (2014) documented its pre-outburst variability. After  $\sim 1.85$  days of its discovery, the nova peaked at  $V \sim 4.43$  on August 16.45 UT (Munari et al. 2013a) and also became an attractive target for amateur astronomers. As a result, a large number of observations with a high cadence in the optical have been performed from  $\gamma$ -rays (Ackermann et al. 2014; Ahnen et al. 2015) to the radio/mm–2 cm wavelengths (Anderson et al. 2013; Chomiuk et al. 2013). A short review of V339 Del was presented by Munari et al. (2015), Shore et al. (2016), Evans et al. (2017), and Chochol et al. (2015). Figure 1

shows the optical light curve (LC) of the nova from day  $\sim 1$  after its explosion (see below) to day  $\sim 1800$ . Main characteristics of V339 Del can be summarized as follows.

**Reddening:** Based on the equivalent width of  $\text{Na I } \lambda 5890$ , Munari et al. (2013b) determined the interstellar reddening to V339 Del to be  $E_{B-V} = 0.18$ , which agrees with the Schlegel et al. (1998) extinction maps as found by Burlak et al. (2015). This value has been used in most papers published to date.

**Distance:** Using the maximum-magnitude-rate-of-decline relation, the distance to the nova was estimated to be 2.7–3.5 kpc (Chochol et al. 2014; Taranova et al. 2014; Burlak et al. 2015). On the basis of near-IR interferometry, Schaefer et al. (2014) determined the pre-maximum expansion rate of the nova fireball, which corresponds to a distance of  $4.54 \pm 0.59 \text{ kpc}$ . In a similar way, but using photometry of the expanding fireball, Gehrz et al. (2015) determined the distance of V339 Del to  $4.5 \pm 0.8 \text{ kpc}$  and the day zero (=the nova explosion) on JD 2,456,518.4 (2013 August 13.9). The distance of 4–4.5 kpc was supported by Shore et al. (2016) by comparing the UV spectrum of the CO nova OS And 1986 and V339 Del taken at a comparable stage of their evolution. Using the distance–extinction relation for the independent measurements of reddening, Özdönmez et al. (2016, 2018) included V339 Del to novae, for which the distance could not be estimated. Finally, the *Gaia* data release 2 catalog presents the distance of  $2130^{+2250}_{-400} \text{ pc}$ , which was classified by Schaefer (2018) as untrustworthy, due to having a parallax error bar  $>30\%$ .

**Temperature:** During the fireball stage (2013 August 14.8–19.9; days 0.9–6.0), when the maximum of the nova radiation was within the optical, Skopal et al. (2014) determined the effective temperature of the WD pseudophotosphere in the range of 6000–12,000 K on the basis of SED models. Comparing photometric *UBVRJHKLM* flux points from the optical maximum (2013 August 15.94 and 16.86; days 2 and 3) to the spectrum of normal supergiants, Taranova et al.

<sup>1</sup> <http://www.aavso.org/apass>

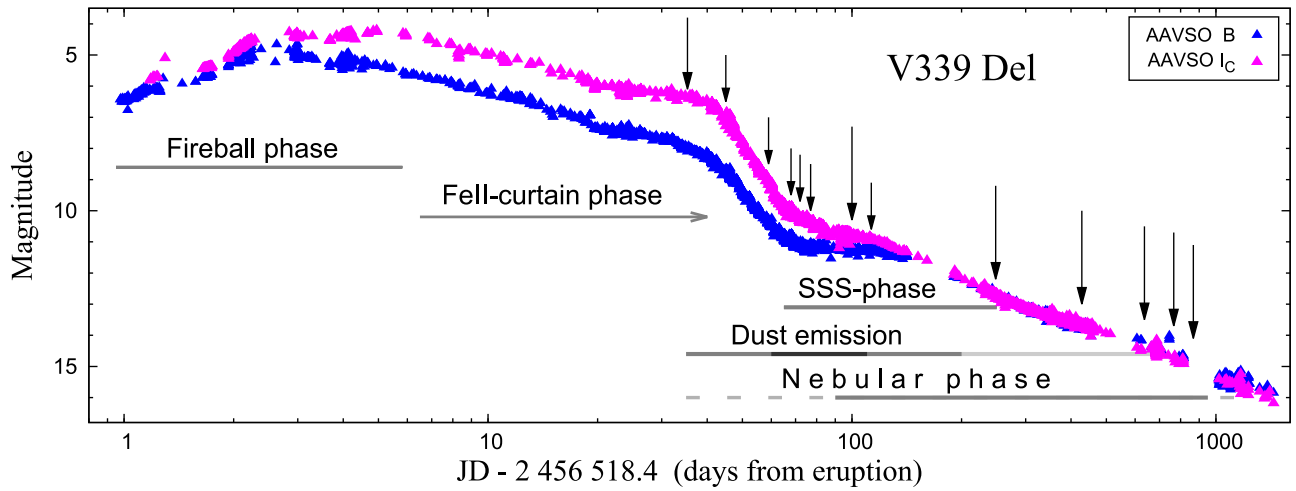


**Figure 1.**  $B$  and  $I_C$  LCs of V339 Del from day 1 to day  $\sim 1500$  from the nova eruption as collected in the AAVSO International Database. Long and short arrows indicate times of the *HST*/STIS and optical/near-IR observations, respectively (Table 1).

(2014) estimated the temperature of the nova to be 13,600 and 9400 K, respectively. During the supersoft source (SSS) phase, on 2013 November 09.75 (day 88), Nelson et al. (2013) estimated a photospheric temperature of the WD of 27 eV ( $\sim 310,000$  K) on the basis of the first high-resolution X-ray spectrum of the nova obtained by the *Chandra* observatory. On 2013 November 21 (day 100), Ness et al. (2013) estimated the temperature of the SSS to be  $\sim 30$  eV ( $\sim 350,000$  K) using the spectrum obtained with *XMM-Newton*.

**Luminosity:** Around the optical maximum, Taranova et al. (2014), Skopal et al. (2014), and Gehrz et al. (2015) estimated the luminosity of the nova to be  $L_{WD} \approx 2.5 \times 10^5 (d/3 \text{ kpc})^2$ ,  $(2.2 \pm 0.2) \times 10^5 (d/3 \text{ kpc})^2$ , and  $\sim 8.3 \times 10^5 (d/4.5 \text{ kpc})^2 L_\odot$ , respectively, i.e., a factor of  $\sim 10$  above the Eddington value. Using the *Hubble Space Telescope* (*HST*)/STIS and optical observations on days 35 and 100, Shore et al. (2016) determined the 1200–7400 Å luminosity to  $(5 \pm 0.5) \times 10^4 L_\odot$ , which is still at or above the Eddington value for a Chandrasekhar-mass WD.

**Dust formation:** On the basis of near-IR photometry, Taranova et al. (2014) indicated a dust emission around 1 month after the optical maximum. On 2013 September 21 (day 38.9) and October 11 (day 58.8), they estimated a color temperature of  $\approx 1500$  and  $\approx 1200$  K, luminosity of  $\sim 4 \times 10^3$  and  $\sim 1.2 \times 10^4 (d/3 \text{ kpc})^2 L_\odot$ , and mass of  $\sim 1.6 \times 10^{24}$  and  $\sim 1.1 \times 10^{25}$  g, respectively. Using the stratospheric observatory *SOFIA* and ground-based infrared observations, Gehrz et al. (2015) revealed the presence of a dust emission with a blackbody temperature of  $850 \pm 40$  K, luminosity of  $\sim 1.7 \times 10^4 (d/4.5 \text{ kpc})^2 L_\odot$ , and mass of  $(1.2 \pm 0.4) \times 10^{-7} M_\odot$  on 2013 November 24.04 (day 102.14). An extensive description of the dust development in V339 Del was presented by Evans et al. (2017), who found that dust formation commenced on day  $\sim 34.75$  at a condensation temperature of  $1480 \pm 20$  K, consistent with graphitic carbon. They determined the rise and fall of the mass of the dust with a maximum at day  $\sim 100$  and the last detection on day 636. Evans et al. (2017) and Shore et al. (2018) considered the possibility of a dust extinction effect in the optical and UV LC, although a strong dust emission in the near-IR was unambiguously indicated (see Section 4.1.3 here).

**The ejecta mass:** Based on the emission measure (EM) from SED models, Skopal et al. (2014) determined the ejecta mass to be  $\sim 1 \times 10^{-5}$  to  $\sim 4.6 \times 10^{-4} M_\odot$  between days 8 and 38, for the volume filling factor  $f = 1$ . Using EM and  $F_{H\beta}$  flux measured over the period of 253–352 days, Tarasova & Skopal

(2016) estimated the ejecta mass to be  $\sim 7 \times 10^{-5} M_\odot$  for  $f = 0.28$ . Gehrz et al. (2015) obtained  $\sim 7.5 \times 10^{-5} M_\odot$  by estimating the cutoff wavelength during the free-free emission phase, and Shore et al. (2016) derived a range of the ejecta mass of  $(2\text{--}3) \times 10^{-5} M_\odot$  for  $f = 0.1$ .

**Veiling the WD photosphere:** It is best documented by the X-ray emission, which is effectively attenuated by the neutral atoms of hydrogen. X-ray radiation from V339 Del was monitored by the *Swift* X-ray telescope with the first detection at harder energies (1–10 keV) on September 19 (day 37), whereas a soft component was detected on 2013 October 13 (day 61), indicating the start of visibility of the WD photosphere (Page et al. 2013). Using the data from 2013 September 19 to 26 (days 37–44), Page & Beardmore (2013) determined the absorbing hydrogen column density,  $N_H = 4.9^{+7.5}_{-3.2} \times 10^{22} \text{ cm}^{-2}$ . A decrease from  $N_H \sim 5 \times 10^{22}$  around day 45 to  $\sim 1.8 \times 10^{22} \text{ cm}^{-2}$  around day 65 was reported by Osborne et al. (2013). On 2013 November 09.75 (day 88), Gattuzz et al. (2018) determined  $N_H \sim 1.23 \times 10^{21} \text{ cm}^{-2}$  using the *Chandra* X-ray spectrum. A summary of the X-ray evolution is given by Shore et al. (2016).

**Geometry of the nova:** Using the near-IR interferometry, Schaefer et al. (2014) indicated a prolate structure of V339 Del already 2 days after the eruption. Modeling the optical/near-IR SED during the first 40 days of the nova evolution, Skopal et al. (2014) suggested a biconical ionization structure of the ejecta with a disk-like H I region encompassing the WD at the orbital plane. During the nebular phase, Tarasova & Skopal (2016) concluded that the ejected material has a disk-polar structure with an orbital inclination of  $\sim 65^\circ$ . Values of  $i = 55^\circ\text{--}35^\circ$  were suggested by Shore et al. (2016). Using high-resolution spectropolarimetric observations, Kawakita et al. (2019) indicated an expanding equatorial torus surrounding the nova photosphere, which changed to a bipolar geometry during a few days of the nova age.

These results were achieved by analyzing the data covering the X-ray, ultraviolet, optical, and near-infrared part of the nova spectrum, in most cases, separately. However, the analysis of multiwavelength observations covering a wide energy range obtained simultaneously at different nova ages can provide a better understanding of the nova evolution.

Accordingly, we reconstruct and model the SED of V339 Del at days when a large fraction of its spectrum is

covered by nearly simultaneous observations taken from day 35 to day 636. In Section 2 we summarize the used observations, while Section 3 describes our analysis and presents the results. Their discussion and summary are found in Sections 4 and 5, respectively.

## 2. Observations

Observations used to model the SED of V339 Del were collected from previous publications and satellite archives. Their timing, spectral range, and sources are introduced in Table 1.

The X-ray fluxes of the SSS continuum were estimated using the RGS spectrum made with *XMM-Newton* at day 100. The spectrum was described by Ness et al. (2013). Because of a rich absorption spectrum and a strong  $C\,V \rightarrow C\,VI$  absorption edge at 31.6 Å, we adopted just the highest peaks in the observed spectrum as the continuum fluxes. We used the figure “P0728200201RGX000FLUXED1003.GIF” available in the *XMM-Newton* Science Archive (ID: 0728200201).

The ultraviolet *HST/STIS* spectra were retrieved from the satellite archive with the aid of the Multimission Archive at the Space Telescope Science Institute (MAST). The spectra from days 35 and 100 were first reported by Shore et al. (2013a, 2013b) and published with a detailed description by Shore et al. (2016), together with the spectrum from day 248.

Low-resolution optical spectra were carried out at the Crimean Astrophysical Observatory (Tarasova & Skopal 2016), at the Fujii Kurosaki Observatory (FKO) by M. Fujii,<sup>2</sup> and from the ARAS database.<sup>3</sup> Spectroscopic observations from the FKO and ARAS were described by Skopal (2014) and Skopal et al. (2017). Additional flux points from the near-IR spectrum obtained at the Mt. Abu observatory were reconstructed from Figure 7 of Evans et al. (2017). Spectroscopic observations were supplemented with the photometric *UBVJHKLM* measurements of Burlak et al. (2015), *KLMNN'* photometry of Gehrz et al. (2015), and *BVR<sub>C</sub>I<sub>C</sub>* magnitudes of Munari et al. (2013a) and/or the AAVSO International Database.<sup>4</sup>

To obtain flux points of the true continuum using the *UBVR<sub>C</sub>* magnitudes, we corrected them for emission lines measured on the low-resolution spectra using the method of Skopal (2007). The contribution of emission lines to the continuum was rather significant, mainly during the nebular phase, because of strong [O III]  $\lambda\lambda 4363, 4950, 5007$  nebular lines and relatively faint continuum (see Table 2). Magnitudes of the true continuum were converted to fluxes according to the calibration of Henden & Kaitchuck (1982) and Bessell (1979). Finally, the *UBVR<sub>C</sub>* continuum flux points were used to scale the relative flux units of the low-resolution spectra to absolute fluxes. Observations were dereddened with  $E_{B-V} = 0.18$  using the extinction curve of Cardelli et al. (1989), and resulting parameters were scaled to a distance of 4.5 kpc (see Section 1).

## 3. Analysis and Results

The primary aim of this paper is to model the SED of V339 Del throughout its iron-curtain phase (day 35), transition to the SSS phase (days 45, 59, 68, 72, and 77), the SSS phase (days 100, 113, and 248), and the nebular phase (days 428 and

636). We achieve this aim by using the method of multi-wavelength modeling the X-ray to IR composite continuum as described by Skopal (2005, 2015a). Its application to the case of classical nova V339 Del is briefly introduced below.

### 3.1. Multiwavelength Modeling the SED

In our modeling we assume that the gamma photons generated in the burning layer on the WD surface are reprocessed by the outside material into softer energies, the distribution of which throughout the electromagnetic spectrum depends on the nova age. Other primary sources of the radiation are not considered.

Basic characteristics of the nova V339 Del, as inferred from its spectrum in different domains and dates (see Section 1), suggest that the continuum consists of three main components of radiation; the stellar component,  $F_{WD}(\lambda)$ , produced by the WD pseudophotosphere, the nebular,  $F_N(\lambda)$ , and the dust,  $F_D(\lambda)$ , components that represent a fraction of the stellar radiation reprocessed by the ejected material. The spectrum of the nova,  $F(\lambda)$ , as observed at Earth, is given by their superposition, i.e.,

$$F(\lambda) = F_{WD}(\lambda) + F_N(\lambda) + F_D(\lambda). \quad (1)$$

During the fireball stage, the outer shell transfers the inner energetic photons to its optically thick/thin interface (i.e., the WD pseudophotosphere), which redistributes their energy chiefly within the optical. The observed spectrum can be compared with an atmospheric model for a star of spectral type A–F, while  $F_N(\lambda)$  and  $F_D(\lambda)$  components can be neglected (see Skopal et al. 2014).

During the transition to harder spectrum, the WD pseudophotosphere shrinks and becomes hotter. As a result, the spectrum shifts the maximum of its SED to shorter wavelengths, and the WD pseudophotosphere ionizes the outer material, giving rise to the nebular emission. Its continuum is approximated by contributions from f–b and f–f transitions in hydrogen plasma, while the stellar continuum and that from the dust are compared with the blackbody radiation at a temperature  $T_{BB}$  and  $T_D$ , respectively.

In the SED-fitting analysis, we compare a grid of models (1) for the given day (see below) with the fluxes of the observed continuum and select that corresponding to a minimum of the reduced  $\chi^2$  function. Because of a rich emission-line spectrum in the UV, it was difficult to identify its true continuum (see, e.g., Figure 2). Therefore, we adopted uncertainties in the measured continuum as high as 10%.

#### 3.1.1. Modeling the Iron-curtain Spectrum on Day 35

Observations used to model the SED of V339 Del at day 35 cover the spectral range from the far-UV to the near-IR (115 nm to 5  $\mu$ m; Table 1). Specific features of the observed spectrum are the flat UV continuum and its attenuation around the Ly $\alpha$  line (Figure 2). The latter can be ascribed to the Rayleigh scattering of the far-UV photons by neutral atoms of hydrogen (e.g., Nussbaumer et al. 1989). It causes the optical depth,  $\tau_{Ray} = \sigma_{Ray}(\lambda) N_H$ , where  $\sigma_{Ray}(\lambda)$  is the Rayleigh cross section for scattering by hydrogen in its ground state (see Equation (5) and Figure 2 of Nussbaumer et al. 1989). Therefore, the attenuation of the continuum by Rayleigh scattering provides an estimate of  $N_H$  between the emitting source and the observer. According to the above-mentioned assumptions and Equations (5) and (11) of Skopal (2005), our Equation (1) can

<sup>2</sup> [http://otobs.org/FBO/fko/nova/nova\\_del\\_2013.htm](http://otobs.org/FBO/fko/nova/nova_del_2013.htm)

<sup>3</sup> [http://www.astrosurf.com/aras/Aras\\_DataBase/Novae/Nova-Del-2013.htm](http://www.astrosurf.com/aras/Aras_DataBase/Novae/Nova-Del-2013.htm)

<sup>4</sup> <https://www.aavso.org/data-download>

**Table 1**  
Log of Observations

Age <sup>a</sup> JD–JD <sub>0</sub>	Date UT YYYY-MM-DD	Julian Date JD 2 456	Region	Observatory/References
34.817	2013 Sep 17.717	553.217	<i>JHKLM</i>	CrAO <sup>b</sup>
35	2013 Sep 17.5	553	<i>UBV</i>	CrAO <sup>b</sup>
35.319	2013 Sep 18.219	553.719	115–289 nm	<i>HST/STIS</i>
35.3	2013 Sep 18.2	553.7	<i>BVR<sub>C</sub></i>	AAVSO <sup>c</sup>
35.7	2013 Sep 18.6	554.1	360–965 nm	FKO <sup>d</sup>
36.82	2013 Sep 19.72	555.22	1.15–2.36 $\mu$ m	Mt Abu <sup>e</sup>
44.616	2013 Sep 27.516	563.016	365–911 nm	FKO <sup>d</sup>
44.869	2013 Sep 27.769	563.269	<i>JHKLM</i>	CrAO <sup>b</sup>
45	2013 Sep 27.5	563	<i>UBV</i>	CrAO <sup>b</sup>
45.194	2013 Sep 28.094	563.594	<i>BVR<sub>C</sub>I<sub>C</sub></i>	<sup>f</sup>
58.788	2013 Oct 11.688	577.188	<i>JHKLM</i>	CrAO <sup>b</sup>
59	2013 Oct 11.5	577	<i>UBV</i>	CrAO <sup>b</sup>
59.572	2013 Oct 12.472	577.972	<i>BVR<sub>C</sub>I<sub>C</sub></i>	<sup>f</sup>
59.637	2013 Oct 12.537	578.037	365–930 nm	FKO <sup>d</sup>
67.832	2013 Oct 20.732	586.232	<i>JHKLM</i>	CrAO <sup>b</sup>
68	2013 Oct 20.5	586	<i>UBV</i>	CrAO <sup>b</sup>
68.318	2013 Oct 21.218	586.718	<i>BVR<sub>C</sub>I<sub>C</sub></i>	<sup>f</sup>
68.582	2013 Oct 21.482	586.982	365–930 nm	FKO <sup>d</sup>
71.817	2013 Oct 24.717	590.217	<i>JHKLM</i>	CrAO <sup>b</sup>
71.875	2013 Oct 24.775	590.275	363–720 nm	ARAS <sup>g</sup>
72	2013 Oct 24.5	590	<i>UBV</i>	CrAO <sup>b</sup>
72.236	2013 Oct 25.014	590.636	<i>BVR<sub>C</sub>I<sub>C</sub></i>	<sup>f</sup>
74.542	2013 Oct 27.442	592.942	370–900 nm	FKO <sup>d</sup>
75.837	2013 Oct 28.737	594.237	<i>BVR<sub>C</sub>I<sub>C</sub></i>	<sup>f</sup>
76.770	2013 Oct 29.670	595.170	<i>JHKLM</i>	CrAO <sup>b</sup>
76.81	2013 Oct 29.71	595.21	<i>UBV</i>	CrAO <sup>b</sup>
77.534	2013 Oct 30.434	595.934	371–900 nm	FKO <sup>d</sup>
77.922	2013 Oct 30.822	596.322	375–740 nm	ARAS <sup>g</sup>
99.845	2013 Nov 21.745	618.245	2.3–3.8 nm	<i>XMM-Newton</i>
99.957	2013 Nov 21.857	618.357	379–736 nm	ARAS <sup>g</sup>
100	2013 Nov 21.5	618	<i>UBV</i>	CrAO <sup>b</sup>
100.0	2013 Nov 21.9	618.4	<i>BVR<sub>C</sub>I<sub>C</sub></i>	AAVSO <sup>h</sup>
100.029	2013 Nov 21.929	618.429	116–307 nm	<i>HST/STIS</i>
100.510	2013 Nov 22.410	618.910	365–911 nm	FKO <sup>d</sup>
101.66	2013 Nov 23.56	620.06	<i>JHK</i>	Mt Abu <sup>i</sup>
102.14	2013 Nov 24.04	620.54	<i>KLMNN</i> <sup>r</sup>	OBO <sup>j</sup>
102.66	2013 Nov 24.56	621.06	1.14–11.6 $\mu$ m	Mt Abu <sup>e</sup>
111.835	2013 Dec 03.735	630.235	375–740 nm	ARAS <sup>g</sup>
112.759	2013 Dec 04.659	631.159	<i>JHKLM</i>	CrAO <sup>b</sup>
113.1	2013 Dec 05.0	631.5	<i>BVR<sub>C</sub>I<sub>C</sub></i>	AAVSO <sup>j</sup>
113	2013 Dec 04.5	631	<i>UBV</i>	CrAO <sup>b</sup>
113.852	2013 Dec 05.752	632.252	662–885 nm	ARAS <sup>g</sup>
248.17	2014 Apr 19.07	766.57	115–570 nm	<i>HST/STIS</i>
248.47	2014 Apr 19.3	766.87	<i>BVR<sub>C</sub>I<sub>C</sub></i>	AAVSO <sup>k</sup>
253.871	2014 Apr 24.771	772.271	400–820 nm	FKO <sup>d</sup>
255.075	2014 Apr 25.975	773.475	380–750 nm	CrAO <sup>l</sup>
428.116	2014 Oct 16.016	946.516	115–307 nm	<i>HST/STIS</i>
428.1	2014 Oct 16.0	946.5	<i>BVR<sub>C</sub>I<sub>C</sub></i>	AAVSO <sup>m</sup>
393.622	2014 Sep 11.522	912.022	400–820 nm	FKO <sup>d</sup>
457.536	2014 Nov 14.436	975.936	430–730 nm	FKO <sup>d</sup>
636.076	2015 May 11.976	1154.476	115–307 nm	<i>HST/STIS</i>
636.1	2015 May 12.0	1154.5	<i>BVR<sub>C</sub>I<sub>C</sub></i>	AAVSO <sup>n</sup>
644.851	2015 May 20.751	1163.251	400–743 nm	FKO <sup>d</sup>



**Table 1**  
(Continued)

Age <sup>a</sup> JD-JD <sub>0</sub>	Date UT YYYY-MM-DD	Julian Date JD 2 456	Region	Observatory/References
766.198	2015 Sep 19.098	1284.598	115–171 nm	<i>HST</i> /STIS
867.126	2015 Dec 29.026	1385.526	115–171 nm	<i>HST</i> /STIS

**Notes.**<sup>a</sup> JD<sub>0</sub> = 2,456,518.4 (2013 August 13.9) is the date of nova explosion.<sup>b</sup> Burlak et al. (2015).<sup>c</sup>  $B = 8.0$ ,  $V = 7.98$ ,  $R_C = 6.44$ .<sup>d</sup> Fujii Kurosaki Observatory (see Skopal et al. 2014).<sup>e</sup> Representative fluxes from Figure 7 of Evans et al. (2017).<sup>f</sup> Munari et al. (2013a).<sup>g</sup> [http://www.astrosurf.com/aras/Aras\\_DataBase/Novae/Nova-Del-2013.htm](http://www.astrosurf.com/aras/Aras_DataBase/Novae/Nova-Del-2013.htm)<sup>h</sup>  $B = 11.24$ ,  $V = 11.20$ ,  $R_C = 10.36$ ,  $I_C = 10.85$ .<sup>i</sup> See Table 4 of Gehrz et al. (2015).<sup>j</sup>  $B = 11.31$ ,  $V = 11.24$ ,  $R_C = 10.43$ ,  $I_C = 10.90$ .<sup>k</sup>  $B = 12.67$ ,  $V = 11.88$ ,  $R_C = 12.02$ ,  $I_C = 12.67$ .<sup>l</sup> Tarasova & Skopal (2016).<sup>m</sup>  $B = 13.72$ ,  $V = 12.62$ ,  $R_C = 12.96$ ,  $I_C = 13.69$ .<sup>n</sup>  $B = 14.22$ ,  $V = 13.25$ ,  $R_C = 13.45$ ,  $I_C = 14.47$ .**Table 2**Corrections  $\Delta m_l = m_{\text{obs}} - m_{\text{cont}}$  of the  $UBVR_C$  Photometry for Emission Lines,  
Where  $m_{\text{cont}}$  Is Magnitude of the True Continuum

Day	$\Delta U_l^a$	$\Delta B_l$	$\Delta V_l$	$\Delta R_{C_l}$
35	$< -0.1$	-0.59	-0.43	-1.18
45	$< -0.06$	-0.68	-0.49	-1.00
59	$< -0.1$	-0.87	-0.57	-1.27
68	$< -0.1$	-1.16	-0.89	-1.36
72	$< -0.06$	-1.06	-0.77	-1.32
77	$< -0.07$	-1.00	-0.78	-1.28
100	$< -0.13$	-0.87	-0.68	-1.12
113	$< -0.07$	-1.09	-0.91	-1.32
248	...	-1.34	-1.39	-1.11
428	...	-1.42	-1.64	-1.18
636	...	-1.37	-1.68	-1.64

**Note.**<sup>a</sup> Spectrum covers only a part of the  $U$ -passband range.

be written in the form

$$F(\lambda) = \theta_{\text{WD}}^2 \pi B_{\lambda}(T_{\text{BB}}) e^{-\sigma_{\text{Ray}}(\lambda) N_{\text{H}}} + k_{\text{N}} \times \varepsilon_{\lambda}(\text{H}, T_{\text{e}}) + \theta_{\text{D}}^2 \pi B_{\lambda}(T_{\text{D}}), \quad (2)$$

where  $\theta_{\text{WD}} = R_{\text{WD}}^{\text{eff}}/d$  is the angular radius of the WD pseudophotosphere, given by its effective radius (i.e., the radius of a sphere with the same luminosity) and the distance  $d$ . The second term at the right is the nebular continuum expressed by its volume emission coefficient,  $\varepsilon_{\lambda}(\text{H}, T_{\text{e}})$  ( $\text{erg cm}^3 \text{s}^{-1} \text{\AA}^{-1}$ ), scaled with the factor  $k_{\text{N}} = \text{EM}/4\pi d^2$ . The emission measure,  $\text{EM} = \int_V n_{\text{p}} n_{\text{e}} dV$ , is given by the proton and electron concentration,  $n_{\text{p}}$  and  $n_{\text{e}}$ , within the volume  $V$  of the ionized hydrogen. Finally, the third term represents the radiation from the dust diluted at Earth with the factor  $\theta_{\text{D}}^2 = (R_{\text{D}}^{\text{eff}}/d)^2$ .

In modeling the global SED, we first fitted 105 UV continuum fluxes from 1185 to 2873 Å and 17 optical fluxes

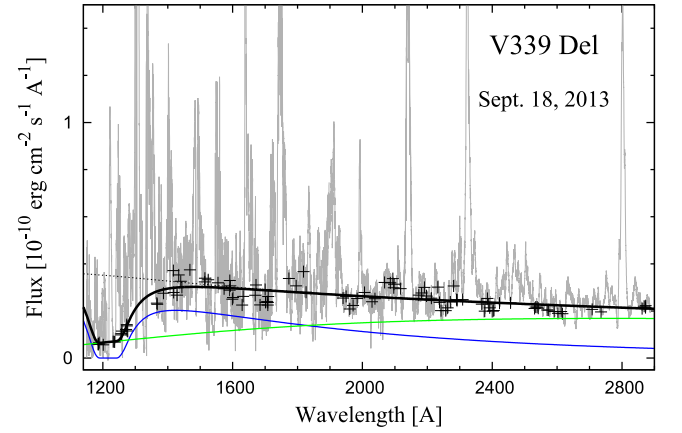


**Figure 2.** *HST*/STIS spectrum of V339 Del on day 35 showing an attenuation of the continuum around the Ly $\alpha$  line due to Rayleigh scattering by atomic hydrogen (Section 3.1.1). The figure represents the UV part of the global SED from Figure 3. The dotted line is the nonscattered continuum. Crosses denote the selected continuum fluxes used to model the SED.

from 3412 to 6918 Å by Equation (2) without the dust component. Second, we filled in the residual flux at *HKLM* flux points with a blackbody radiation to estimate parameters of the dust emission. In this way we obtained parameters  $\theta_{\text{WD}}$ ,  $T_{\text{BB}}$ , and  $N_{\text{H}}$  for the stellar component,  $T_{\text{e}}$  and  $k_{\text{N}}$  for the nebular component, and  $\theta_{\text{D}}$  and  $T_{\text{D}}$  for the dust component of radiation. The luminosity of the WD pseudophotosphere is given as

$$L_{\text{WD}} = 4\pi d^2 \theta_{\text{WD}}^2 \sigma T_{\text{BB}}^4. \quad (3)$$

Finally, the model SED clearly extracts the unidentified source of emission around 1  $\mu\text{m}$  (see Figure 3), whose presence was already noted by Gehrz et al. (2015).

### 3.1.2. Modeling the Optical/near-IR Spectrum during the Transition to the SSS Phase

This period in the nova evolution is characterized by a steep decline of the optical brightness between days  $\sim 35$  and  $\sim 72$

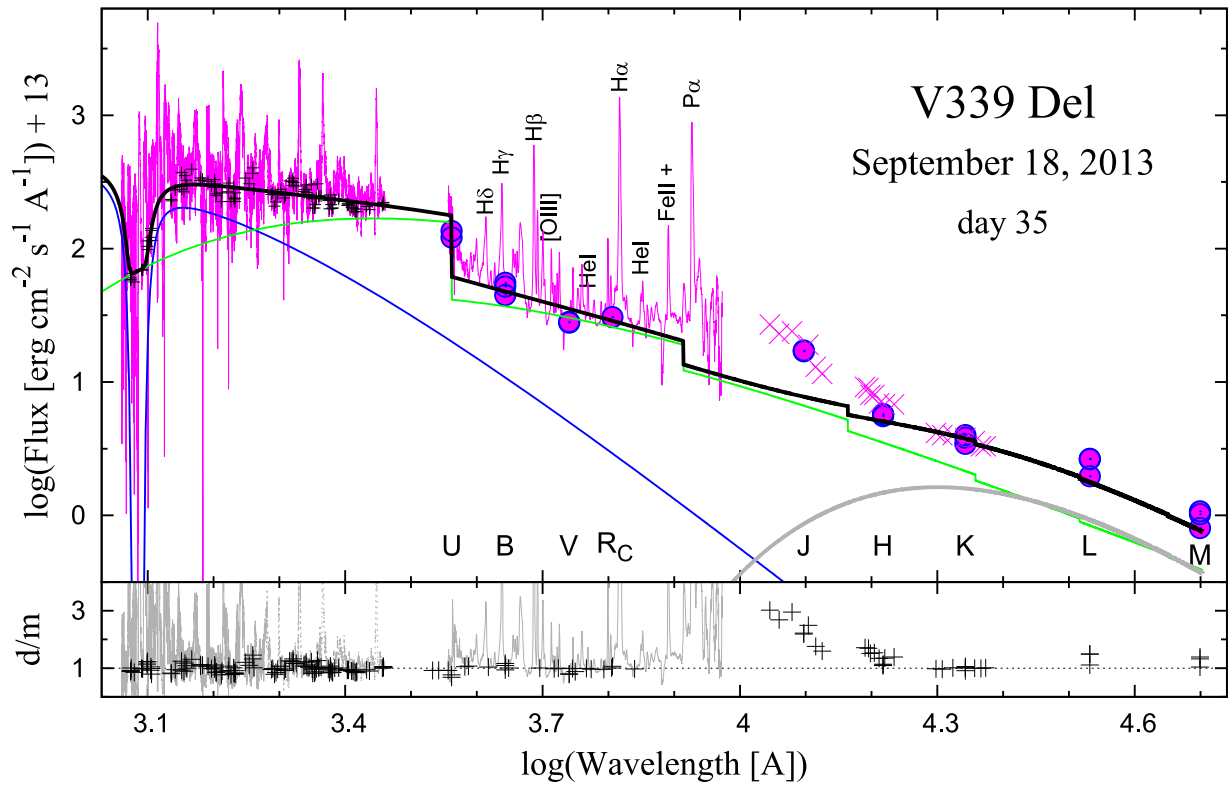


**Figure 3.** Observed (in magenta: spectrum and photometric flux points) and model (thick black line) SEDs of V339 Del from 0.12 to 5  $\mu\text{m}$  on day 35 with corresponding data-to-model ratios (d/m). The model SED is given by a superposition of the radiation from the WD pseudophotosphere (blue line), the nebula (green line), and the dust (gray line) according to Equation (2). The model unambiguously extracts an unidentified source of radiation around 1  $\mu\text{m}$ .

and the presence of a strong near-IR emission. Our observations cover the nova age between days 45 and 113 and consist of low-resolution optical spectra and *UBVR<sub>C</sub>I<sub>C</sub>JHKLM* photometry (Table 1). During this period, the optical/near-IR continuum is dominated by the nebular emission and that from the dust. Therefore, we used these components to determine the model SED,

$$F(\lambda) = k_N \times \epsilon_\lambda(H, T_e) + \theta_D^2 \pi B_\lambda(T_D), \quad (4)$$

where the variables  $k_N$ ,  $T_e$ ,  $\theta_D$ , and  $T_D$  are explained in Section 3.1.1. Dominance of the nebular continuum and the dust emission in the optical and in the near-IR, respectively, allows us to determine both the components independently. Similarly to Equation (3), we determine the effective dust luminosity as  $L_D = 4\pi d^2 \theta_D^2 \sigma T_D^4$ . Finally, we formally included the stellar component with  $T_{\text{BB}} \equiv 10^5$  K and scaling, subtly influencing the short-wavelength part of the optical. Models are shown in Figure 10.

### 3.1.3. Modeling the SSS Spectrum on Days 100 and 248

At the nova age of 100 days, we modeled its SED from the supersoft X-rays to the IR/N band (2.3 nm to 11  $\mu\text{m}$ ; Table 1). The spectrum is characterized by very high X-ray fluxes, a steep UV/optical continuum, and a large emission bump in the IR. In principle, the procedure of modeling is the same as in the previous case, but the observed X-ray fluxes have to be corrected for bound-free absorptions within the interstellar (ISM) and circumstellar (CSM) matter. In this case the first

term of Equation (1) is expressed as

$$F_{\text{WD}}(\lambda) = \theta_{\text{WD}}^2 \pi B_\lambda(T_{\text{BB}}) e^{-\sigma_X(\lambda) N_H}, \quad (5)$$

where  $\sigma_X(\lambda)$  is the total cross section for photoelectric absorption per hydrogen atom (e.g., Cruddace et al. 1974). Here we used the *tbabs* absorption model for ISM composition with abundances given by Wilms et al. (2000) (e.g.,  $\log(A_{\text{CI}}) + 12 = 8.38$ ).

In the spectrum at day 100, we simultaneously fitted 13 absorbed X-ray continuum fluxes from 23 to 38  $\text{\AA}$ , 105 dereddened UV fluxes from 1161 to 3066  $\text{\AA}$ , and 13 optical fluxes from 3554 to 8095  $\text{\AA}$ , searching for parameters  $\theta_{\text{WD}}$ ,  $T_{\text{BB}}$ ,  $N_H$ ,  $T_e$ , and  $k_N$ . The dust component was determined independently, because of a significant excess of its emission with respect to the nebular and stellar component in the IR. Comparing blackbody radiation to fluxes from 1.1 to 11.6  $\mu\text{m}$  revealed the presence of two components of the dust emission. The larger and cooler component ( $\lambda_{\text{max}} \sim 3.4 \mu\text{m}$ ) was already identified by Gehrz et al. (2015), while the smaller and hotter one ( $\lambda_{\text{max}} \sim 1.7 \mu\text{m}$ ) is constrained by our global SED (see Figure 4).

During the late SSS phase on day 248, the *Swift*-XRT count rate was reduced by a factor of  $\sim 1000$  relative to day 100. The continuum used to model the SED was determined by the UV *HST*/STIS and optical spectra (1150–8200  $\text{\AA}$ ; Table 1). Strong far-UV continuum and its steep slope toward the longer wavelengths suggest a dominant contribution from a hot WD in the far-UV, while a relatively flat and strong optical continuum constrains the presence of a hot nebular radiation. Therefore, we fitted the observed SED using Equation (2) restricted to the

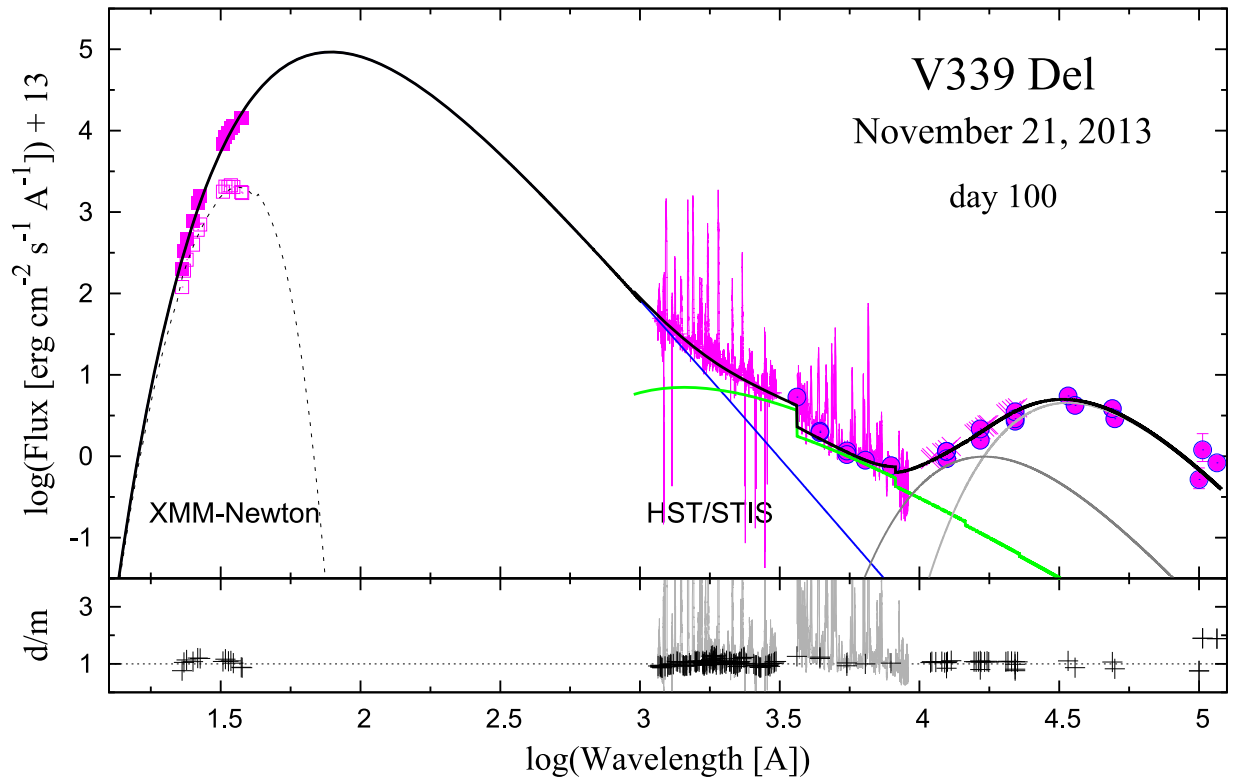


**Figure 4.** Observed and model SED of V339 Del from 2.3 nm to 11  $\mu\text{m}$  on day 100. Open and filled squares are the measured and unabsorbed X-ray fluxes, respectively. Denotation of lines and points as in Figure 3.

stellar and nebular component of radiation only, i.e.,

$$F(\lambda) = \theta_{\text{WD}}^2 \pi B_{\lambda}(T_{\text{BB}}) + k_{\text{N}} \times \varepsilon_{\lambda}(H, T_{\text{e}}), \quad (6)$$

where variables  $\theta_{\text{WD}}$ ,  $T_{\text{BB}}$ ,  $T_{\text{e}}$ , and  $k_{\text{N}}$  are described in Section 3.1.1. Here we fitted 81 UV/optical continuum fluxes from 1159 to 5620  $\text{\AA}$  of the *HST/STIS* spectrum with function (6). In this way we determined parameters  $\theta_{\text{WD}}$ ,  $T_{\text{e}}$ , and  $k_{\text{N}}$  for the fixed  $T_{\text{BB}}$ . Under the condition that the radiation from the WD pseudophotosphere fits the UV/optical SED and generates the *Swift*-XRT count rate, it was possible to estimate the value of  $T_{\text{BB}}$  independently (see Appendix A in detail). For the observed rate of  $\sim 0.025$  photons  $\text{s}^{-1}$  (see Figure 1 of Shore et al. 2016) and the flux, e.g.,  $F_{\text{WD}}^{248}(1195 \text{ \AA}) = 1.37 \times 10^{-12} \text{ erg cm}^{-2} \text{ s}^{-1} \text{ \AA}^{-1}$ , we obtained  $T_{\text{BB}}^{248} = 225 \pm 5 \text{ kK}$ . The model SED for day 248 is shown in Figure 5.

#### 3.1.4. Modeling the Nebular Spectrum on Days 428 and 636

During the nebular phase, the spectrum was modeled in the same way as that from day 248, because their SED profile was of the same type (see Figure 5). They differed only in the continuum level, which decreased by a factor of  $\sim 3$  and  $\sim 7$  on days 428 and 636 with respect to day 248. In both cases we estimated the lower limit of  $T_{\text{BB}}$  to be  $\sim 100,000 \text{ K}$ , as given by the presence of the N V  $\lambda\lambda 1238.8, 1242.8$  resonance doublet ( $\chi \sim 97.9 \text{ eV}$ ; see Section 3.2), and its upper limit to be  $\sim 160,000 \text{ K}$ , at which the WD radiation is just outside of the *Swift*-XRT energy range.

The observed and model SEDs are depicted in Figures 3–5 and 10, and the corresponding parameters are listed in Table 3. In spite of the fact that only static blackbody-like models with

nebular hydrogen continuum are used, the resulting models express well the measured *global* SED.

### 3.2. Temperature of the WD Pseudophotosphere

The WD temperature in novae depends on their age. Its determination is not often unique. Here we introduce cases for days 35, 100, and 248, when the SED models allow us to determine a reliable value of  $T_{\text{BB}}$ .

#### 3.2.1. $T_{\text{BB}}$ on Day 35

At the nova age of 35 days, the unusually flat UV continuum and the slope of the optical to near-IR continuum are given by superposition of the stellar radiation from a relatively warm WD pseudophotosphere and a large amount of a hot nebular radiation (Figure 3, Table 3). Such a special profile of the UV–IR SED provides an unambiguous solution. However, the observed WD radiation is not capable of giving rise to the large amount of the nebular emission. The observed,  $\sim 31,000 \text{ K}$  warm, stellar pseudophotosphere (Table 3) generates the flux of hydrogen-ionizing photons  $L_{\text{H}} \sim 9.5 \times 10^{47} \text{ s}^{-1}$ , which can produce a maximum of  $\text{EM} = L_{\text{H}}/\alpha_{\text{B}}(H, T_{\text{e}}) \sim 8.1 \times 10^{60} \text{ cm}^{-3}$  (see Section 3.3 in detail) for the total hydrogen recombination coefficient  $\alpha_{\text{B}}(H, T_{\text{e}}) = 1.18 \times 10^{-13} \text{ cm}^3 \text{ s}^{-1}$  (e.g., Nussbaumer & Vogel 1987). However, this value is a factor of  $\sim 23$  below the measured quantity of  $1.9 \times 10^{62} \text{ cm}^{-3}$  (Table 3). This implies that there is a powerful ionizing source in the center radiating at the ionization temperature  $T^{\text{i.s.}} > T_{\text{BB}}$ , which is not seen directly by the outer observer at day 35.

The lower limit of  $T^{\text{i.s.}}$  is given by the presence of an ion in the nebula with the highest ionization energy  $\chi_{\text{max}}$ , because it requires photons with  $h\nu > \chi_{\text{max}}$ . According to Mürset & Nussbaumer (1994),  $T^{\text{i.s.}} = 1000 \times \chi_{\text{max}}$ , where  $\chi_{\text{max}}$  is in eV.

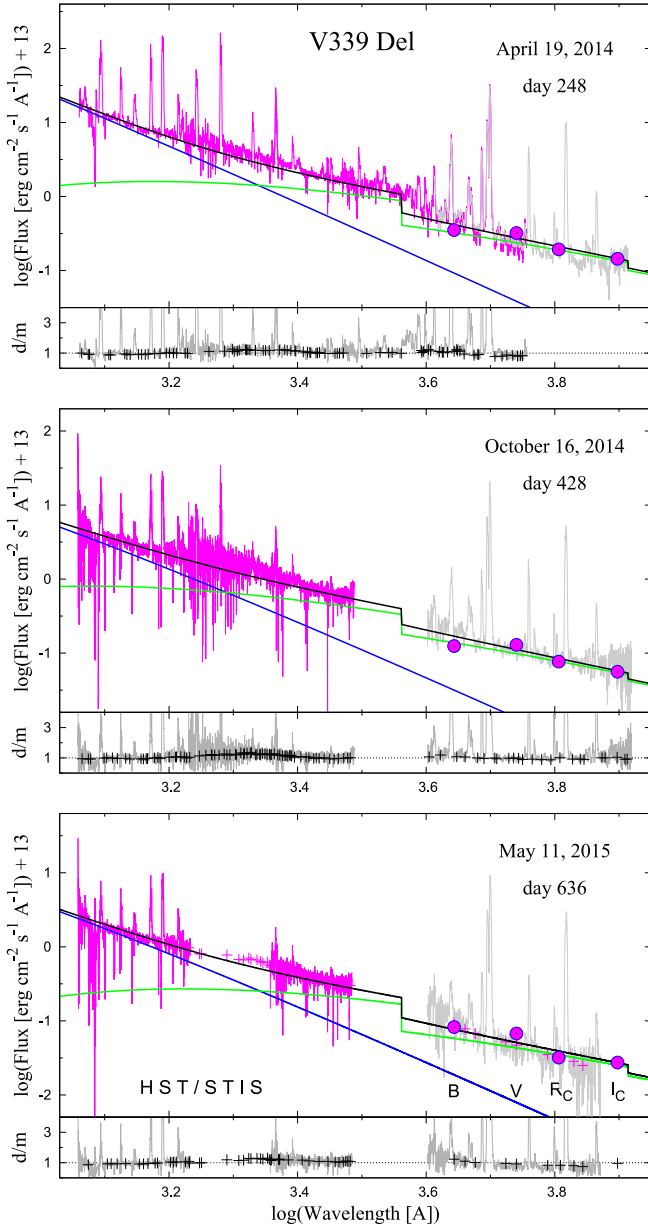


**Figure 5.** UV/optical SEDs on days 248, 428, and 636 of the nova age. Denotation of lines and points as in Figure 3.

The presence of the N IV  $\lambda 1486$  ( $\chi \sim 77.5$  eV) emission line suggests  $T_{i.s.} > 77,000$  K. On the other hand, absence of the N V  $\lambda \lambda 1238.8, 1242.8$  ( $\chi \sim 97.9$  eV) resonance doublet in emission (see Shore et al. 2016) suggests  $T_{i.s.} < 98,000$  K. Thus, the temperature of the ionizing source on day 35 is in the range of 77,000–98,000 K.

### 3.2.2. $T_{BB}$ on Day 100

At the nova age of 100 days, we determined  $T_{BB}$  directly by modeling the X-ray to IR continuum under the assumption that both X-ray and far-UV fluxes are emitted by the WD pseudophotosphere (see Section 3.1.3). Our value of  $T_{BB} = 369 \pm 8$  kK is close to the estimate of  $\sim 350$  kK made by Ness et al. (2013) on the basis of solely the X-ray fitting and assuming  $N_H = 1 \times 10^{21} \text{ cm}^{-2}$ . We note that determination of the effective temperature of the hot WD photosphere would require exact fitting of its rich absorption-line spectrum using a

non-LTE model atmosphere analysis (e.g., Lanz et al. 2005). This challenging task is beyond the scope of this paper.

### 3.2.3. $T_{BB}$ on Day 248 and Beyond

During the late SSS phase (day 248),  $T_{BB}$  was determined by modeling the UV/optical SED with the aid of the measured *Swift*-XRT count rate (Section 3.1.3, Appendix A). In this way, we obtained  $T_{BB} = 227 \pm 5$  kK. A relatively small error is constrained by having defined the WD spectrum from both the short- and the long-wavelength side, similarly to day 100.

During the nebular phase (days 428 and 636), only the range of possible  $T_{BB}$  can be estimated on the basis of the presence of emission lines with the highest ionization potential and the condition of no emission within the *Swift*-XRT energy range (Section 3.1.4).

### 3.3. Luminosity of the Burning WD

The bolometric luminosity,  $L_{WD}$ , of the hot burning WD at day 35 can be estimated only indirectly, under the assumption that the total flux of hydrogen-ionizing photons,  $L_H$ , is converted into the nebular radiation. Then, having the quantity of EM from observations, we can estimate the corresponding  $L_{WD}$  for the given temperature of the ionizing source.

Assuming further that the nebula is characterized by a constant electron temperature,  $T_e$ , we can approximate the equilibrium condition between  $L_H$  and the rate of recombinations in the nebula as

$$L_H = \alpha_B(H, T_e) EM, \quad (7)$$

where  $\alpha_B(H, T_e)$  is the recombination coefficient to all but the ground state of hydrogen (i.e., Case B). The quantity of  $L_H$  is given by the temperature and luminosity of the ionizing source, while the value of EM is determined by the model SED. According to Skopal et al. (2017), the luminosity of the ionizing source, which produces the observed EM, can be expressed as

$$L_{WD} = \alpha_B(H, T_e) EM \frac{\sigma T_{BB}^4}{f(T_{BB})}, \quad (8)$$

where the function  $f(T_{BB})$  determines the flux of ionizing photons emitted by the  $1 \text{ cm}^2$  area of the ionizing source ( $\text{cm}^{-2} \text{ s}^{-1}$ ). Figure 6 shows Equation (8) for the observed  $EM = 1.9 \times 10^{62} \text{ cm}^{-3}$ . The temperature range of the ionizing source, 77,000–98,000 K (Section 3.2), corresponds to  $L_{WD} \sim 1.1 \times 10^{39} \text{ erg s}^{-1}$ .

Optically thick conditions, where the nebular continuum grows from complete absorption of stellar photons with  $\lambda < 912 \text{ \AA}$ , are of critical importance for the validity of the above approach. A signature of the optically thick conditions is the presence of elements at very different ionization states in the spectrum (see Kaler & Jacoby 1989, and references therein). On day 35, emission lines of N II–IV, C I–IV, Si IV, He I–II, H I, O I, [O I]  $\lambda 6300$ , and Fe II as indicated in the UV–optical spectrum of V339 Del (see Figures 3, 8, and A.1 of Shore et al. 2016) suggest that the nebula is rather ionization bounded, that is, the stellar radiation below  $912 \text{ \AA}$  ( $< 13.6$  eV) is absorbed within the nebula. Also, no detection of ionizing photons on day 35 within the *Swift*-XRT energy range (see Figure 1 of Shore et al. 2016) supports this case.

During the SSS phase, direct observation of a significant fraction of the hydrogen-ionizing photons in the form of



**Table 3**  
Physical Parameters of Individual Components of Radiation in the Spectrum of V339 Del from SED Models (Section 3.1)

Age (days)	$N_H$ ( $10^{21} \text{ cm}^{-2}$ )	WD Pseudophotosphere			Nebula		Dust			$\chi^2_{\text{red}}/\text{dof}$
		$T_{\text{BB}}$ (kK)	$R_{\text{WD}}^{\text{eff}}$ ( $R_{\odot}$ )	$\log(L_{\text{WD}})$ ( $\text{erg s}^{-1}$ )	$T_e$ (kK)	EM ( $10^{60} \text{ cm}^{-3}$ )	$T_D$ (K)	$R_D^{\text{eff}}$ ( $R_{\odot}$ )	$L_D$ ( $L_{\odot}$ )	
35	$110^{+20}_{-60}$	$31 \pm 1.5$ 77–98	$5.9 \pm 0.8$ 1.7–1.1	$38.05 \pm 0.11$ 39.0–39.1 <sup>a</sup>	$26 \pm 2$	$190 \pm 15$	$1450 \pm 100$	$890 \pm 110$	$3120 \pm 700$	1.69/121
45					$30 \pm 5$	$84.8 \pm 9$	$1250 \pm 80$	$2760 \pm 250$	$16600 \pm 3200$	...
59					$30 \pm 5$	$14.5 \pm 2$	$1050 \pm 60$	$5200 \pm 500$	$29000 \pm 5500$	...
68					$40 \pm 7$	$9.7 \pm 1$	$1000 \pm 60$	$5030 \pm 480$	$22700 \pm 4400$	...
72					$50 \pm 10$	$8.48 \pm 0.9$	$900 \pm 70$	$5800 \pm 500$	$20100 \pm 3900$	...
77					$50 \pm 10$	$8.0 \pm 1$	$1800 \pm 150$	$460 \pm 50$	$2030 \pm 350$	...
							$850 \pm 70$	$6200 \pm 530$	$17800 \pm 3400$	
							$1800 \pm 150$	$530 \pm 60$	$2630 \pm 440$	
100	$1.02 \pm 0.1$	$369 \pm 8$	$0.20 \pm 0.02$	$39.43 \pm 0.11$	$50 \pm 10$	$8.48 \pm 0.8$	$850 \pm 70$	$5630 \pm 700$	$14840 \pm 3000$	0.89/126
113					$50 \pm 10$	$6.1 \pm 0.7$	$1700 \pm 140$	$464 \pm 55$	$1600 \pm 330$	...
							$850 \pm 70$	$5300 \pm 450$	$13100 \pm 2600$	
							$1550 \pm 130$	$560 \pm 65$	$1600 \pm 300$	
248	$0.8 \pm 0.4$	$227 \pm 5$	$0.16 \pm 0.01$	$38.36 \pm 0.12$	$48 \pm 8$	$1.96 \pm 0.5$				1.50/77
428	$0.8 \pm 0.4$	$100^b$	0.15	36.87	$60 \pm 10$	$0.91 \pm 0.1$				1.27/94
		$160^b$	0.10	37.38	$60 \pm 10$	$0.95 \pm 0.1$				1.62/94
636	$0.8 \pm 0.2$	$100^b$	0.11	36.64	$43 \pm 7$	$0.34 \pm 0.04$				1.85/51
		$160^b$	0.08	37.12	$46 \pm 7$	$0.39 \pm 0.04$				2.27/51
766	$0.9 \pm 0.2$									
867	$0.8 \pm 0.3$									

**Notes.**

<sup>a</sup> From the measured EM (see Sections 3.2 and 3.3).

<sup>b</sup> Fixed value (see Sections 3.2).

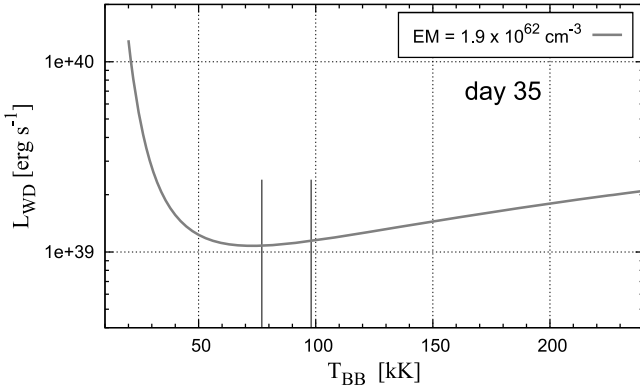


**Figure 6.** WD luminosity as a function of the WD temperature scaled with the EM measured on day 35 (Equation (8)). Vertical bars limit the range of the temperature (see Section 3.2.1).

supersoft X-ray emission (Figure 4) means that the nebula of V339 Del became particle bounded. As a result, its EM significantly dropped with respect to the value from day 35 (Table 3). The method above (Equation (8)) is not applicable for the spectrum from day 100. Instead, we can directly integrate the stellar component of radiation given by the X-ray/near-IR model SED, which yields  $L_{\text{WD}} = (2.7 \pm 0.7) \times 10^{39} (d/4.5 \text{ kpc})^2 \text{ erg s}^{-1}$ . This value justifies those obtained indirectly using the nebular component of radiation.

Luminosities during the late SSS and nebular phase rely on estimates of the corresponding  $T_{\text{BB}}$  (see Section 3.2). Figure 12 shows evolution of the WD luminosity as a function of the nova age. It demonstrates a long-lasting super-Eddington luminosity of the burning WD in V339 Del at least for the first 100 days of its life.

### 3.4. Veiling of the WD by Neutral Hydrogen

Apart from b–f absorptions of X-ray photons by hydrogen atoms, the hydrogen column density between the WD pseudophotosphere and the observer,  $N_H$ , can be also determined from attenuation of the far-UV continuum around the Ly $\alpha$  line, which is caused by Rayleigh scattering on H atoms (Section 3.1.1). On day 35, the continuum depression around Ly $\alpha$  was stretched up to  $\sim 1400 \text{ \AA}$  (Figure 2), which corresponds to  $N_H = 1.1^{+0.2}_{-0.6} \times 10^{23} \text{ cm}^{-2}$ , in agreement with the following estimates from X-ray observations (Figure 8). Such a high value of  $N_H$  is in major part given by its CSM component. It is of interest to note that signatures of Rayleigh scattering, corresponding to similar values of  $N_H$ , developed also in the spectra of the symbiotic nova PU Vul and classical nova V723 Cas during their transition to a harder spectrum (see Figure 1 of Skopal 2014).

On day 100, having observed the supersoft X-ray component of the nova spectrum, we determined  $N_H$  directly by modeling the SED (Section 3.1.3) to  $\sim 1.0 \times 10^{21} \text{ cm}^{-2}$ . This value corresponds to the interstellar component, because it is relevant to the extinction to the nova,  $E_{B-V} = 0.18 \text{ mag}$  (e.g., Diplás & Savage 1994). Comparison of the far-UV spectrum with the Rayleigh scattered model continuum also supports this value of  $N_H$ , although the influence of the Ly $\alpha$  emission is significant (see the top panel of Figure 7).

During the following observations (days 248, 428, 636, 766, and 867), attenuation of the far-UV continuum by Rayleigh scattering was clearly recognizable, corresponding just to the ISM component of  $N_H \sim 8 \times 10^{20} \text{ cm}^{-2}$  with uncertainties up to 50% (Table 3, Figure 8), depending on the signal-to-noise ratio.<sup>5</sup>

<sup>5</sup> To suppress the noise, we smoothed the spectra using average values of fluxes within  $0.25 \text{ \AA}$ .

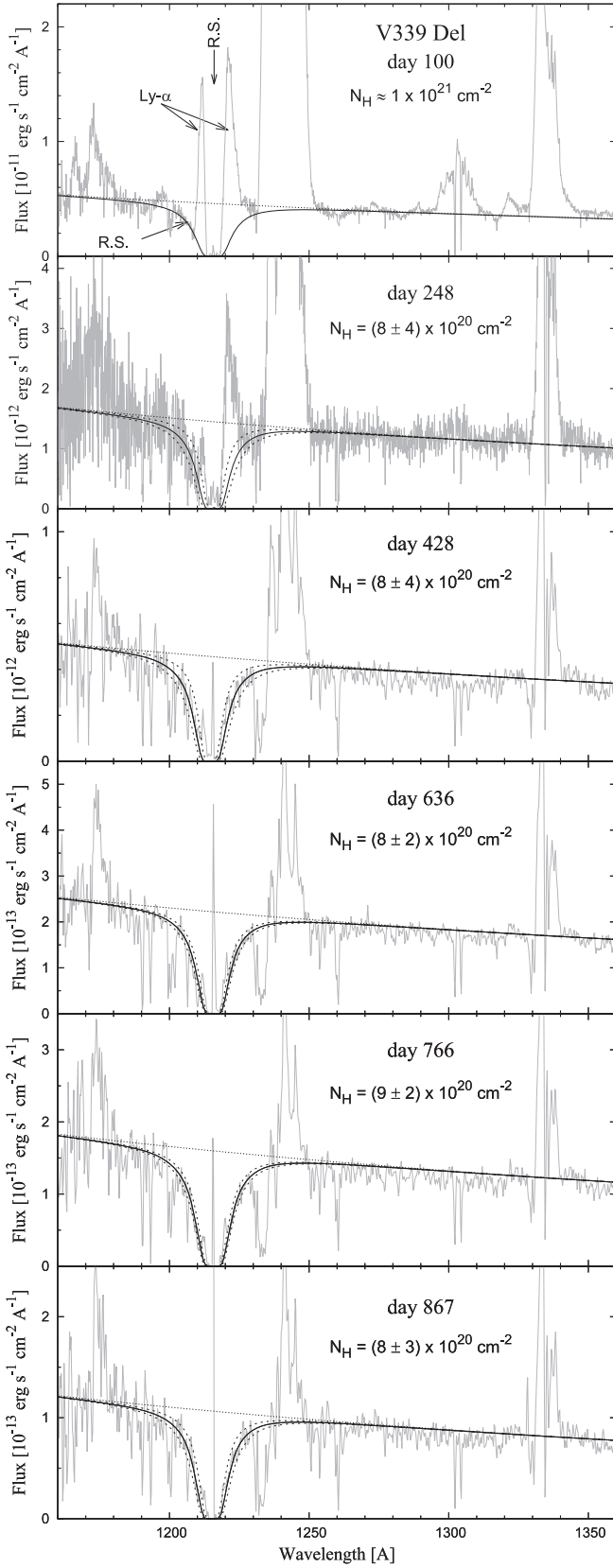


**Figure 7.** Hollow in the continuum around Ly $\alpha$  observed during the SSS and nebular phase and its match by Rayleigh scattering (full and dashed lines; R.S.). Dotted lines above the hollow represent the nonscattered continuum.

Therefore, in contrast to Equation (2), we attenuated the total model continuum,  $F(\lambda)$ , with the function  $\exp[-\sigma_{\text{Ray}}(\lambda)N_{\text{H}}]$ , because the only present ISM component of  $N_{\text{H}}$  attenuates both the stellar and the nebular radiation from the nova. As a result, the rest flux around the reference wavelength is close to zero (see Section 4.4).

Our fits of the continuum attenuation around Ly $\alpha$  by Rayleigh scattering are shown in Figure 7, while the evolution of  $N_{\text{H}}$  along the nova age is depicted in Figure 8.

## 4. Discussion

### 4.1. Transition from the Iron-curtain to the SSS Phase

Here we discuss the steep decline of the optical brightness, EM, and  $N_{\text{H}}$  between days 35 and 72. With the aid of SED models we endeavor to find its origin.

#### 4.1.1. Stopping the Mass Outflow from the WD

SED models show that the nebular component of radiation dominates the near-UV to optical spectrum for the nova age  $\gtrsim 35$  days (Figures 3–5 and 10). It represents a fraction of the WD’s radiation converted by the ejecta into the nebular radiation via f–f and f–b transitions. Its flux is given by the EM of the ionized gas (see Section 3.1.1, Equation (2)). Therefore, knowing the EM from the model SED, we can estimate the mass of the ionized ejecta and the corresponding mass-loss rate from the WD,  $\dot{M}_{\text{WD}}$ . According to the simplified approach of Skopal et al. (2014),  $\dot{M}_{\text{WD}}$  can be expressed as

$$\dot{M}_{\text{WD}} = \mu m_{\text{H}} v_{\text{exp}} \left[ \epsilon 4\pi \text{EM} \left( \frac{1}{R_{\text{WD}}^{\text{eff}}} - \frac{1}{R_{\text{neb}}} \right)^{-1} \right]^{1/2} \text{ g s}^{-1}, \quad (9)$$

where  $\mu$  is the mean molecular weight and  $m_{\text{H}}$  is the mass of the hydrogen atom, while  $v_{\text{exp}}$  denotes the expansion velocity of the ejecta, and  $\epsilon = 2\Delta\Omega/4\pi$  is the filling factor, where  $\Delta\Omega < \pi$  is the opening angle of the expanding ionized region, whose EM is integrated from  $R_{\text{WD}}^{\text{eff}}$  to the outer radius of the nebula,  $R_{\text{neb}}$ .

For a mean expansion velocity of 750 km s $^{-1}$  derived from the half-width at half-maximum of the hydrogen emission lines (Tarasova & Skopal 2016; Evans et al. 2017) and parameters of the model SED,  $R_{\text{WD}}^{\text{eff}}$  and EM (Table 3), we obtain  $\dot{M}_{\text{WD}} = 8.7 \times 10^{-5} M_{\odot} \text{ yr}^{-1}$  for day 35, while on day 72, when the drop in the brightness and in the EM came to a standstill (Figure 8),  $\dot{M}_{\text{WD}}$  decreased by a factor of  $\sim 25$ , to  $3.4 \times 10^{-6} M_{\odot} \text{ yr}^{-1}$ . We assumed  $R_{\text{WD}}^{\text{eff}} \ll R_{\text{neb}}$  and  $\epsilon = 1$ , which corresponds to a maximum of  $\dot{M}_{\text{WD}}$ .

Thus, the rapid decline of the EM during the brightness fall ( $\sim$ days 35–72) was caused by a significant stopping-down of the mass outflow from the WD.

#### 4.1.2. On the Nature of the Steep Brightness Decline

This period in the nova evolution is characterized by a significant decrease of its optical brightness by  $\Delta B \approx 3$  mag and  $\Delta I_{\text{C}} \approx 4$  mag between days 35 and 72 (see Figure 1). Simultaneously,  $N_{\text{H}}$  decreased from  $\sim 1 \times 10^{23}$  to its ISM

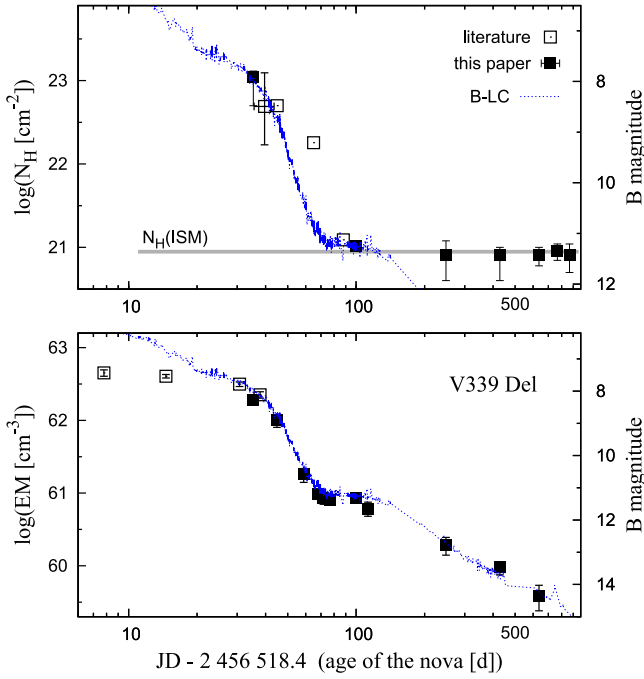


**Figure 8.** Top: column density of hydrogen atoms,  $N_H$ , along the nova age. The horizontal line corresponds to the ISM value (Section 3.4). Bottom: same as the top panel, but for the EM. The  $B$ -LC (blue line) is scaled to both parameters on the y2-axis (Section 4.1.2). Our data are from Table 3.

value of  $\sim 1 \times 10^{21} \text{ cm}^{-2}$  and EM decreased from  $\sim 2 \times 10^{62}$  to  $\sim 8.5 \times 10^{60} \text{ cm}^{-3}$  (Figure 8).

According to SED models (Figures 3, 4 and 10), the fall of the optical brightness prior to the SSS phase was caused by the decrease of both the nebular and the stellar continuum. A distinctive *increase* in  $T_{\text{BB}}$  and  $T_e$  to day 100 shifted the maximum of the stellar component to shorter wavelengths and made both the continua much steeper than on day 35, which yields  $\Delta I_C > \Delta B$ . This is because the nebular component,  $F_N(\lambda) = \text{EM}/4\pi d^2 \times \varepsilon_\lambda(H, T_e)$  (Section 3.1.1), dominates the optical, and thus we can estimate the value of the drop as

$$\Delta m_\lambda = -2.5 \log \left[ \frac{\text{EM}^{35} \varepsilon_\lambda^{35}(H, T_e)}{\text{EM}^{72} \varepsilon_\lambda^{72}(H, T_e)} \right], \quad (10)$$

where indices 35 and 72 denote quantities corresponding to these days of the nova age. For values of EM,  $T_e$  in Table 3, and the continuum-emission coefficient  $\varepsilon_\lambda(H, T_e)$  introduced by, e.g., Brown & Mathews (1970), Equation (10) yields  $\Delta B = 3.5 \pm 0.05$  and  $\Delta I_C = 3.8 \pm 0.05$  mag, in agreement with the observed values.

Simultaneous fading of both the  $N_H$  and EM between days 35 and 72 was caused by a drop in the  $\dot{M}_{\text{WD}}$  (Section 4.1.1), which considerably lowers particle concentration of the nebula and thus its absorbing ability and emissivity. As a result, the ejecta became optically thinner for harder photons, which led to shrinking of the WD pseudophotosphere, the increase of its temperature, and, consequently, an increase of the electron temperature of the irradiated nebula (Table 3). Therefore, the very steep optical brightness decline with the power of  $-5$  to  $-7$  in fluxes (see Figure 9) was in part caused by shifting of both components of radiation from the optical to shorter wavelengths. The nova settled at the SSS phase.

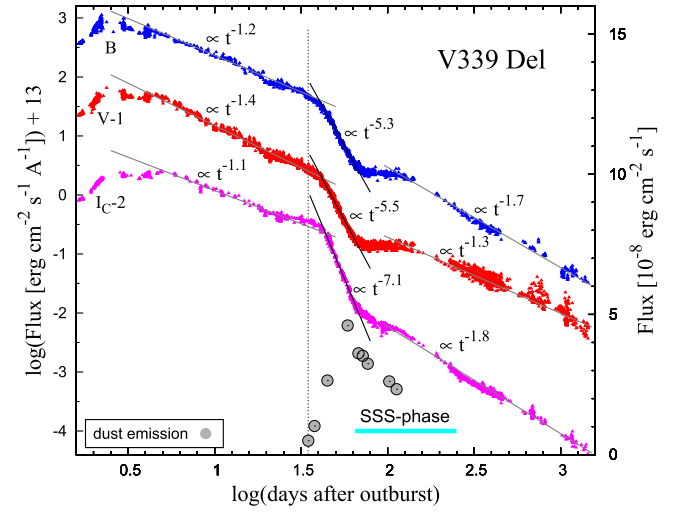


**Figure 9.** Fluxes corresponding to  $B$ ,  $V$ ,  $I_C$  magnitudes according to conversion of Henden & Kaitchuck (1982). Power-law fits are for 5–40 day, 42–62 day, and  $\sim 150$ –1500 day parts of the LC. Measured flux of the dust emission is scaled on the y2-axis (data from Table 3). The dotted line denotes its first detection.

#### 4.1.3. Is There a Dust Extinction along the Line of Sight?

Based on SED models, we suggested that the simultaneous drop in the stellar brightness, EM, and  $N_H$  during the transition from day 35 to the SSS phase is caused by stopping down the mass loss from the WD (Sections 4.1.1 and 4.1.2). On the other hand, Evans et al. (2017) ascribed the decline in the visual LC to dust extinction. However, the following facts do not support this view:

1. The observed fall of the flux in the  $I_C$  band ( $\lambda_{\text{eff}} = 7900 \text{ \AA}$ ) is steeper and larger than in the  $B$  band ( $\lambda_{\text{eff}} = 4400 \text{ \AA}$ ). Figure 9 demonstrates this case. The slope of flux  $F_{I_C} \propto t^{-7.1}$ , while  $F_B \sim F_V \propto t^{-5.4}$ , which corresponds to  $\Delta I_C > \Delta B(\Delta V)$  during the flux fall (see also Equation (10)). Such behavior contradicts attenuation of the light by the dust (e.g., Cardelli et al. 1989). For a comparison, the wavelength dependence of dust extinction was clearly demonstrated for the nova V5668 Sgr (see Figure 3 of Gehrz et al. 2018).
2. No dust extinction along the line of sight is indicated by multiwavelength modeling the SED before, during, and after the steep flux decline. All the corresponding models (see Figures 3, 4, and 10) fit observations corrected solely with the ISM component of the dust extinction,  $E_{B-V} = 0.18$  mag.
3. The IR excess produced by the dust emission was clearly measured already on day 34.8, i.e., around 6–7 days prior to the steep flux decline (Figure 9).

Shore et al. (2018) suggested that a short-lasting dip in the *Swift*-UV LC around day 77 (see their Figure 11) signals formation of dust, although there is no counterpart seen in the optical LC (see, e.g., precise LCs of Munari et al. 2015). However, our optical/near-IR SED models indicate creation of the dust more than 1 month prior to the dip in the UV continuum. A rapid growth of the near-IR emission happened already between days 35 and 45, with a maximum around day 59 (Figures 9 and 10). It is of interest to note that the UV dip coincides with emergence of the rapid variation in the *Swift*-

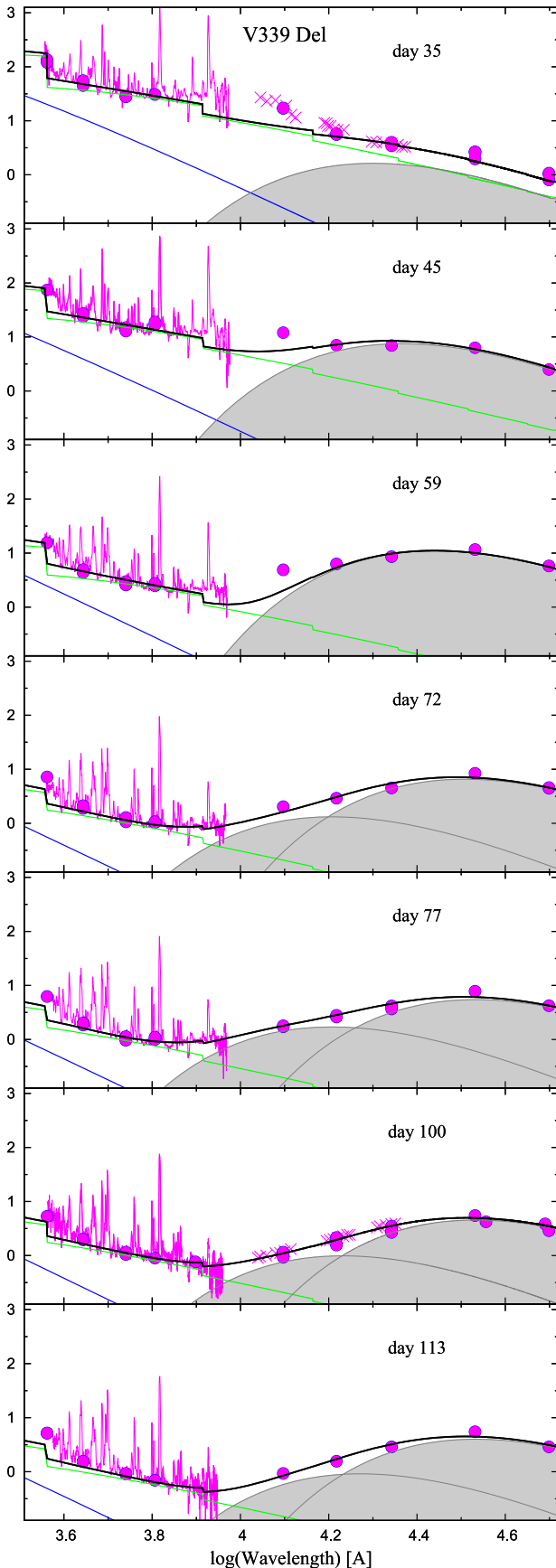


**Figure 10.** Optical/near-IR SEDs during the transition from the iron-curtain to the SSS phase, when a strong dust emission developed (gray area; Section 3.1.2). Denotation of lines and points as in Figure 3. Fluxes are in  $10^{-13} \text{ erg cm}^{-2} \text{ s}^{-1} \text{ Å}^{-1}$ .

XRT count rate (see Figure 1 of Shore et al. 2016), which suggests their common origin. According to SED models, the X-ray to UV continuum ( $\lambda \lesssim 2000 \text{ Å}$ ) is dominated by the radiation from the WD photosphere, and thus these events probably reflect its variability. However, the optical is contaminated by the nebular continuum, which overlays the presumable variation of the stellar component. This suggests that the agent (dense clumps?) responsible for the changes in the X-ray/UV continuum is located above the ionizing source but below the extended nebula ( $EM \sim 10^{61} \text{ cm}^{-3}$ ), whose light cannot vary on the timescale of days.

To answer the question of this section, it is also important to consider the effect of hard radiation on the survival of dust in the nova environment. This effect was discussed in detail by Fruchter et al. (2001), who considered grain heating and grain charging as two principal mechanisms responsible for dust destruction. Using their approach, Evans et al. (2017) found that charging of grains by X-radiation is more than sufficient to shatter the grains around V339 Del already before day 100. Also, Gehrz et al. (2018) showed that the X-ray fluence is sufficient to destroy the dust in the nova V5668 Sgr if the grains are exposed to X-rays for  $\sim 1$  month. On the other hand, to explain the asymmetry in the line profiles with a suppressed red wing, Shore et al. (2018) state that there is no need to invoke dust destruction at late times in either V5668 Sgr or V339 Del, even under irradiation by the X-ray and EUV from the central star.<sup>6</sup>

According to the arguments above (points 1–3 of this section) and our interpretation (Section 4.1.2), we conclude that there is no detectable dust extinction along the line of sight during the steep drop in the star’s brightness. Hence, the presence of a strong near-IR emission throughout this period (Figure 10) and far beyond it (Evans et al. 2017) requires a nonspherical arrangement of the dust region within the nova ejecta.

#### 4.2. On the Structure of the Nova Ejecta

Already 2 days after the explosion, observations indicated a prolate structure of the nova. Later evolution suggested a biconical, disk-polar ionization structure of the ejecta (see Section 1). Figure 11 shows a sketch for the nova ejecta as can be inferred from SED models on days 35 and 100, just before and after the sudden drop in the star’s brightness. It is similar to that derived from radio imaging of V959 Mon (see Figure 3 of Chomiuk et al. 2014), specifying some details of its inner part.

##### 4.2.1. The Oblate Shape of the WD Pseudophotosphere

On day 35, the flat UV continuum is a result of superposition of a relatively warm stellar and a strong nebular component of radiation (Figure 3). The former is not capable of giving rise to the observed nebular emission, and thus the latter signals the presence of a strong ionizing source in the system with  $T^{i.s.} > T_{BB}$ , which is not seen directly by the observer (see Section 3.2.1). Such a type of spectrum is called the two-temperature-type UV spectrum. It is often observed during Z And-type outbursts of symbiotic binaries, where it is followed by emergence of an attenuation of the far-UV continuum by Rayleigh scattering on a few times  $10^{22}$ – $10^{23}$

<sup>6</sup> However, a depression of the red wings due to blocking a fraction of the radiation from the receding ejecta by the disk (see Section 4.1. of Skopal et al. 2006) was not considered.



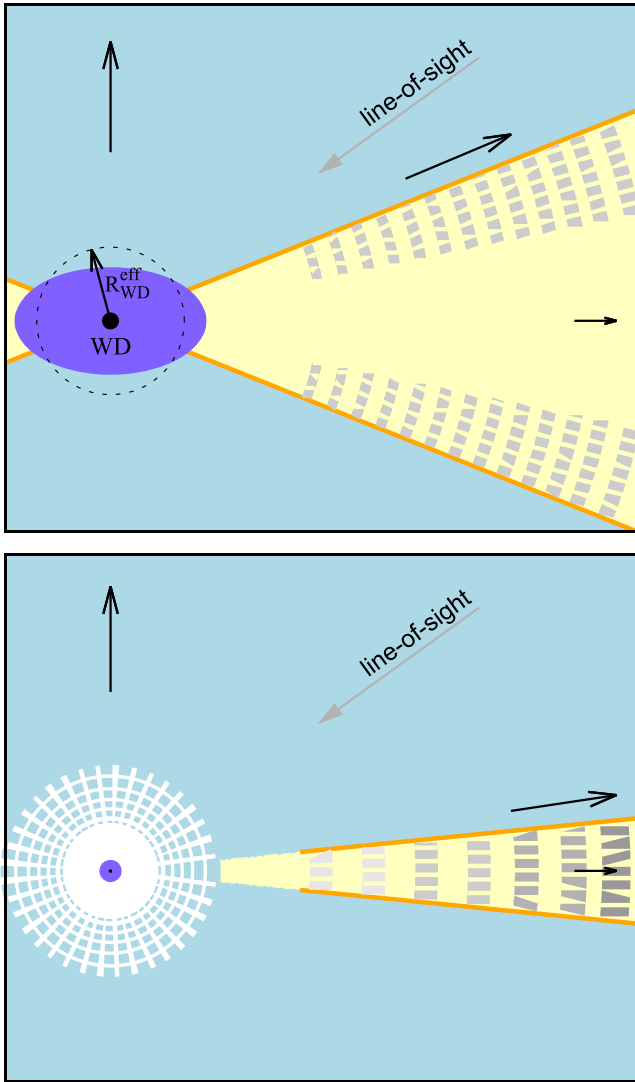


**Figure 11.** Sketch for nova ejecta inferred from the model SED on days 35 (top) and 100 (bottom). A slow equatorially concentrated outflow (yellow area) can be formed due to rotation of the WD (Cariková & Skopal 2012) and/or by the interaction of the binary stars with the ejecta (Livio et al. 1990). A higher-velocity and more spherical wind (light blue) is powered by the WD. Bow shocks are produced between both the ejecta (orange lines), where dust can form (gray elements; Section 4.2.3). Just before the steep drop in the star’s brightness, the day 35 model SED indicates an oblate shape of the WD pseudophotosphere (dark blue; Section 4.2.1). After the optical drop, the day 100 model SED indicates stopping the WD wind (white; Section 4.1.1) and dusty disk with a hotter and cooler dust (light- and dark-gray elements; Sections 4.2.2 and 4.2.3). A similar structure was inferred from radio imaging of V959 Mon (see Figure 3 of Chomiuk et al. 2014).

hydrogen atoms (see Section 5.3.4., Figure 27, and Table 4 of Skopal 2005). The corresponding SED is explained by a disk-like structure of the WD pseudophotosphere, whose hotter regions with smaller radii are located at/around its poles and, vice versa, cooler regions with larger radii are located toward the WD equator.

Accordingly, the day 35 model SED of V339 Del suggests such an oblate shape of the WD pseudophotosphere (see Figure 11, top) with relevant nonspherical temperature distribution: the observed  $\sim 31$  kK warm pseudophotosphere and 77–98 kK hot central ionizing source (Section 3.2.1). A higher-density stellar wind in the direction of the observer creates the optically thick/thin interface (i.e., the WD

pseudophotosphere) at a larger distance from the wind origin than at its pole. The wind gives rise to a large amount of CSM above it as indicated by the high value of  $N_H$ , which precludes detection of the supersoft X-rays on day 35.

#### 4.2.2. Dusty Disk during the SSS Phase

The day 100 model SED indicates the simultaneous presence of a strong dust emission and luminous high-temperature supersoft X-ray source in the nova. This fact and no detection of the dust extinction along the line of sight (Section 4.1.3) constrain a nonspherical distribution of the dust within the ejecta. According to the biconical ionization structure of the ejecta with an equatorially concentrated outflow (see Figure 9 of Skopal et al. 2014), we will assume that the dust is located within the cooler and denser equatorial zone, where it is shielded from the hard radiation of the WD (see Figure 11). Shaping of the dust into a flat disk/ring around the heating source is also supported by the long-lasting presence of the dust, to  $\sim$ day 680 (Evans et al. 2017), because its radial thickness for the incident radiation is extremely large ( $\approx R_D^{\text{eff}} \sim 10^{14}$  cm; Table 3).

From day 72, the SED models indicate two components of the dust emission (Figure 10), whose size and radiation are very different. Their effective radii,  $R_D^{\text{eff}}$ , and luminosities,  $L_D$ , are given in Table 3. Approximating their geometry with a flat disk seen under the inclination angle  $i$ , their radius  $R_{\text{disk}} = R_D^{\text{eff}} / \sqrt{\cos(i)}$  and the luminosity  $L_{\text{disk}} = L_D / \cos(i)$  (see Appendix B). Location of the dust in the ejecta is sketched in Figure 11.

#### 4.2.3. Formation of the Dust in the Equatorial Disk

Recently, Derdzinski et al. (2017) proposed that dust formation occurs in the cool, dense shell behind the powerful radiative shocks within nova outflows. Assuming that the TNR is first accompanied by a slow ejection of mass focused in the equatorial plane and then followed by a second ejection with a higher velocity and more spherical geometry, the subsequent collision between both the ejecta produces strong shocks in the equatorial plane. As the shocked gas cools by a factor of  $\sim 10^3$  and increases its density with a similar factor, it represents an ideal environment for dust forming.

Plausibility of this interpretation for V339 Del is supported by the following observations.

1. The primary outflow with the expansion velocity of  $1600\text{--}700$  km s $^{-1}$  was followed by the secondary outflow in the form of a wind accelerating to  $\sim 2700$  km s $^{-1}$  just after the fireball phase ( $\gtrsim$ day 6, see Figures 7 and 8 of Skopal et al. 2014).
2. Detection of the  $\gamma$ -ray emission near the optical peak with a maximum around day 8 (see Ackermann et al. 2014; Ahnen et al. 2015) confirmed the presence of shocks developing between the fast and slow flows (see also Cheung et al. 2016; Li et al. 2017; orange lines in Figure 11 here).
3. Kawakita et al. (2019) attributed the change in the effective geometry of V339 Del (see Section 1) to the collision between the slowly expanding torus and the faster nova wind, which is consistent with the model proposed by Li et al. (2017).
4. According to Hachisu & Kato (2018), the slow decline of the optical flux  $F \propto t^{-1}$ , observed for some novae during the early stage of their evolution, can be caused by the

shock interaction that decelerates the ejecta, resulting in a slower decrease of its density and thus the flux with time  $t$ . After the shock breakout, the slope changes to  $F \propto t^{-1.6}$ . Such slopes of the nova decay are similar to those observed for V339 Del (see Figure 9), which is consistent with the presence of a shock deceleration mechanism.

The hotter, smaller, and less luminous dust component may represent just the innermost part of the dusty equatorial ring (light-gray elements in Figure 11, bottom). Progressively harder radiation of the WD heats up the dust and destroys it gradually toward to its outer rim. The temperature of the hotter dust,  $\sim 1700$  K, which is just above the upper limit for the condensation of graphitic carbon ( $\sim 1690$  K)—the main component of the dust in V339 Del (see Evans et al. 2017)—is consistent with its destruction. As a result, the dust emission will gradually weaken.

Finally, we note that the cooler, equatorially concentrated outflow could be formed during outburst by compression of the mass outflow (wind) toward the equatorial plane due to rotation of the WD as was suggested for Z And–type outbursts of symbiotic binaries by Cariková & Skopal (2012).<sup>7</sup> This mechanism (originally introduced by Bjorkman & Cassinelli 1993) naturally gives rise to the biconical ionization structure of the ejecta, whose opening is related to the mass-loss rate from the WD as  $\dot{M}_{\text{WD}}^{-2}$ . Thus, the decrease of  $\dot{M}_{\text{WD}}$  (see Section 4.1.1) will cause opening of the ionized zone and narrowing of the dense dusty disk at the equator, whose innermost part will move away from the central WD (see Figure 1 of Cariková & Skopal 2012).

### 4.3. Long-lasting Super-Eddington Luminosity

#### 4.3.1. The Case of V339 Delphini

Figure 12 shows evolution of  $L_{\text{WD}}$  along the nova age, from the first observations around day 1 to the last model SED on day 636. During the early evolution, from day  $\sim 1$  to day  $\sim 2$ , the real increase of  $L_{\text{WD}}$  from  $\sim 3.5 \times 10^{38}$  to  $\sim 1.8 \times 10^{39} \text{ erg s}^{-1}$  was indicated by the increase of fluxes from the WD pseudophotosphere, whose maximum SED was located in the optical (see Figure 1 of Skopal et al. 2014). After the following decrease to  $\sim 1.2 \times 10^{39} \text{ erg s}^{-1}$  during day  $\sim 3$ , the  $L_{\text{WD}}$  persisted at a high level of  $(1\text{--}2) \times 10^{39} \text{ erg s}^{-1}$  until day 100, when the WD radiation was determined by the X-ray/near-IR model SED (Figure 4). Such a high luminosity was probably prolonged to day 150, when *Swift*-XRT still detected strong supersoft X-ray emission at the same level as on day 100. A significant decrease of  $L_{\text{WD}}$  and  $T_{\text{BB}}$  was first determined on day 248 (Appendix A) as indicated by weakening of the X-ray source and the decrease of the UV fluxes. Following measurements on days 428 and 636 confirmed gradual fading of  $L_{\text{WD}}$  to  $\sim 10^{37} \text{ erg s}^{-1}$  (Section 3.3).

Using the indirect method in deriving  $L_{\text{WD}}$ , the principal assumption is that the nebula is optically thick for the Lyman continuum photons of the ionizing source. Before the SSS phase, observations support this assumption (see Section 3.3). Therefore, we estimated  $L_{\text{WD}}$  also for EM determined by Skopal et al. (2014) for days 7.8–37.8 (see their Table 3). We adopted  $T_{\text{BB}} \equiv 73,000$  K, at which the ionizing source

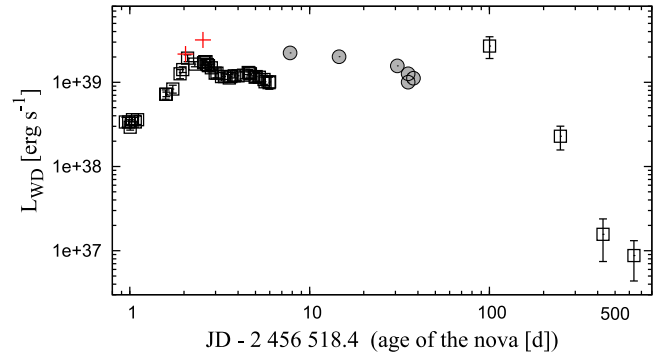


**Figure 12.** Evolution of the WD luminosity along the nova age. Squares denote values derived from the stellar component of radiation in the SED models (see Skopal et al. 2014, for days  $< 7$ ; this paper for days  $> 99$ ), while circles represent those obtained from the nebular component (Section 3.3). Red crosses are values published by Taranova et al. (2014) and Gehrz et al. (2015).

produces the maximum of photons capable of ionizing hydrogen for a given luminosity.

At the end of the fireball stage ( $\sim$ day 6), values of  $L_{\text{WD}}$  from the WD pseudophotosphere were lower by the fraction generating the nebular radiation that started to be visible at this time (see Figures 1 and 2 of Skopal et al. 2014). Because the following values of  $L_{\text{WD}}$  from the EM could be overestimated owing to collisional ionization, but also underestimated owing to measuring only the optically thin part of the nebula, it is not possible to determine errors for indirectly estimated values of  $L_{\text{WD}}$ .

Nevertheless,  $L_{\text{WD}}$  given by the stellar component of radiation in the day 100 model SED confirms previous values from EM, and thus the long-lasting super-Eddington luminosity for, at least, the first 100 days of the nova life (Figure 12).

#### 4.3.2. When Can the Super-Eddington Luminosity Be Indicated?

In most cases the super-Eddington luminosity is indicated at the optical maximum, when the absolute magnitude of numerous (fast) novae is  $M_{\text{V,B}} \lesssim -7$  (e.g., Livio 1992; Della Valle & Livio 1995; Shafter et al. 2009; Shaviv & Dotan 2012). This is because, during this very early stage of evolution, most novae reprocess a significant fraction of their radiation into the optical, which allows a direct estimate of their luminosity. Usually, a simple blackbody fit to the multicolor photometry provides a rough estimate of the nova luminosity (e.g., Gehrz et al. 2015, for V339 Del).

Later, when the maximum SED is shifting to shorter wavelengths and the optical is dominated by the nebular emission, it is not possible to determine directly the nova luminosity by fitting only the observed UV–optical continuum (e.g., the day 35 model SED here). This possibility arises again during the SSS phase, when the supersoft X-ray and far-UV fluxes define the WD spectrum from both the short- and long-wavelength sides (here, the day 100 model SED). This can reveal a startling result that the super-Eddington state of some novae lasts for a long time after their eruption (Section 4.3.1). To prove this case, at least for the optically bright novae, measurements of X-ray and far-UV fluxes during the SSS phase are required.

#### 4.3.3. Current View on Super-Eddington Luminosity

Our findings of the super-Eddington luminosity for V339 Del are not consistent with theoretical modeling that

<sup>7</sup> However, binary components orbiting within the nova envelope can also focus the mass toward the orbital plane (Livio et al. 1990; Lloyd et al. 1997).

the super-Eddington phase can persist only for a short time at the beginning of the nova eruption (e.g., Prialnik & Kovetz 1995; Yaron et al. 2005; Starrfield et al. 2008). On the other hand, the long-term super-Eddington luminosity was observationally documented for more novae, for example, nova FH Ser (Friedjung 1987), LMC 1988 #1 (Schwarz et al. 1998), LMC 1991 (Schwarz et al. 2001), RS Oph (Skopal 2015b, 2015c), and nova SMCN 2016-10a (Aydi et al. 2018), which thus support our finding for V339 Del. Also, the summary of Shafter et al. (2009) that there are 12, 26, and 5 novae in our Galaxy, M31, and LMC, respectively, that have reached absolute visual magnitude  $M_V \lesssim -9.0$  suggests luminosities highly above the Eddington limit.

The super-Eddington state of novae was investigated by Shaviv (1998), who suggested a decrease of the effective opacity of the inhomogeneous atmosphere of novae, which increases the Eddington luminosity well above its standard value, calculated for the Thomson-scattering opacity (see also Shaviv & Dotan 2010, 2012).

Based on remarkable correlation between the  $\gamma$ -ray and optical LCs of the luminous ( $\approx 10^{39}$  erg s $^{-1}$ ) nova ASASSN-16ma, Li et al. (2017) suggested that the majority of the optical light comes from reprocessed emission from shocks rather than the WD. The  $\gamma$ -ray–optical brightness correlation was indicated at/after the optical maximum (see their Figure 1), when the dense slow ejecta ahead of the shocks reprocesses their radiation into the optical, giving rise to the observed optical luminosity of  $\approx 10^{39}$  erg s $^{-1}$ . In this way, the authors replace the standard model, in which most of ultraviolet and/or optical emission in novae is the result of outward diffusion of the radiation from the WD (e.g., Yaron et al. 2005), and state that the shock-driven emission provides an explanation for super-Eddington luminosity observed for many novae. However, at late stages, particularly during the SSS phase, the super-Eddington luminosity is indicated by directly measuring the photospheric radiation transferred through the atmosphere of the WD, which thus leaves the long-standing mystery of why many novae exceed the Eddington limit for a long time still open.

#### 4.3.4. On the Long-lasting Super-Eddington Luminosity

A possibility of how to keep a nova at the super-Eddington state for a long time is to fuel the burning WD also after the eruption. Here, by analogy with the Z And-type outbursts, a disk-like reservoir of mass can be created at the equatorial plane during the outburst (see the last paragraph of Section 4.2.3). Due to the presence of a strong central source of radiation (the burning WD), the inner parts of the disk can be accreted again onto the WD via the radiation-induced warping, which prolongs the period with a high luminosity, until depletion of the inner disk. This event can be accompanied by formation of bipolarly collimated high-velocity outflow (see Skopal et al. 2018, and references therein). The long-term super-Eddington luminosity of the recurrent nova RS Oph (Skopal 2015b, 2015c) and the bipolar jet-like collimated outflow observed in its spectrum during days 10–30 after the 2006 outburst maximum (see Skopal et al. 2008) suggest that this mechanism could work also during outbursts of classical novae. However, multiwavelength observations along evolution of other novae and their theoretical modeling are needed to justify applicability of this accretion mechanism for classical novae.

#### 4.4. Measuring $N_H$ from Rayleigh Scattering

In some recent papers on novae the authors used the Voigt function to model the interstellar Ly $\alpha$  absorption (e.g., Mason et al. 2018). Instead, we modeled the attenuation around the Ly $\alpha$  line by Rayleigh scattering on atomic hydrogen. We justify our approach as follows.

Rayleigh scattering by neutral atoms of hydrogen represents the process where an incident photon raises an electron from the ground state to the intermediate state, followed by the direct return of the electron to the original state, re-emitting a photon of the same energy (e.g., Nussbaumer et al. 1989). The strength of Rayleigh scattering is determined by the value of  $N_H$ , and its profile is given solely by its cross section (Section 3.1.1). As the cross section has a “singularity” near the wavelength of a Lyman line (e.g., Figure 2 of Nussbaumer et al. 1989), the rest flux around the reference wavelength is close to zero. For example,  $N_H = 1 \times 10^{21}$  cm $^{-2}$  creates an absorption core with zero rest flux,<sup>8</sup> an FWHM of  $\sim 15$  Å, and wings expanding approximately to  $\pm 25$  Å around the Ly $\alpha$  line (see Figure 7). Therefore, in spite of small kinematic motions of atoms in the ISM, Rayleigh scattering can create a very broad hollow with expanding wings around the Ly $\alpha$  line, depending only on the quantity of  $N_H$ .

### 5. Summary

In this paper we continued the work of Skopal et al. (2014) by multiwavelength modeling the SED of V339 Del from the iron-curtain phase on day 35 to the nebular phase on day 636 (Section 3, Figures 3–5 and 10). Pivotal models were made for days 35 and 100, when the large and most important part of the nova spectrum is covered by simultaneous observations (Table 1). In this way we determined physical parameters of the stellar, nebular, and dust components of radiation (Table 3) and obtained new information on the nova evolution. The main results can be summarized as follows:

1. During the transition from the iron-curtain to the SSS phase (days 35–72), the steep decline in the optical brightness by 3–4 mag, the fall of  $N_H$  by its CSM component from  $\sim 10^{23}$  to  $\sim 10^{21}$  cm $^{-2}$ , and the decrease of EM from  $\sim 2 \times 10^{62}$  to  $\sim 8.5 \times 10^{60}$  cm $^{-3}$  (Figure 8) were caused by stopping down the wind from the WD (Section 4.1).
2. SED models on days 35 and 100 revealed the long-lasting super-Eddington luminosity that persists at the level of  $(1\text{--}2) \times 10^{39}$  (d/4.5 kpc) $^2$  erg s $^{-1}$  from  $\sim$ day 2 (the optical maximum) to at least day 100 of the nova life (Section 4.3, Figure 12).
3. The day 35 model SED indicates an oblate shape of the WD pseudophotosphere, whose hotter part with a smaller radius is located around the poles, while the cooler regions with larger radii are stretched toward the WD equator (Section 4.2.1). The indicated dust can be formed within a slow equatorially concentrated outflow as a result of its interaction with the fast nova wind (Section 4.2.3, Figure 11). The dust emission reached its maximum around day 59 (Figures 9 and 10).

On day 100, the coexistence of both the strong dust

<sup>8</sup> Contribution of the scattered photons to the line of sight, which can be of a few percent (Schmid 1995), is not detectable on our spectra.



emission and the luminous high-temperature WD photosphere confirms the disk-like shaping of the dust even during the SSS phase (Section 4.2.2). The indicated hotter dust is located at the inner part of the dusty ring, where the hard WD radiation destroys the dust gradually toward its outer rim. In this way the disk can preserve the dust within the ejecta for a long time (Section 4.2.3, Figure 11).

The author thanks the anonymous referee for constructive suggestions that led to improving the manuscript. *HST* spectra presented in this paper were obtained from the Mikulski Archive for Space Telescopes (MAST). MAST is located at the Space Telescope Science Institute (STScI). STScI is operated by the Association of Universities for Research in Astronomy, Inc., under NASA contract NAS5-26555. This work is based in part on observations obtained with *XMM-Newton*, an ESA science mission with instruments and contributions directly funded by ESA Member States and NASA. Mitsugu Fujii, Taya Tarasova, and David Boyd are thanked for acquisition of their spectra at the Fujii Kurosaki Observatory, the Crimean Astrophysical Observatory, and the West Challow Observatory, respectively. We also acknowledge the variable-star observations from the AAVSO International Database contributed by observers worldwide and used in this research. This work was supported by the Slovak Research and Development Agency under contract No. APVV-15-0458, by the Slovak Academy of Sciences grant VEGA No. 2/0008/17, and by the realization of the project ITMS No. 26220120029, based on the supporting operational Research and development program financed from the European Regional Development Fund.

## Appendix A

### Temperature of the WD Pseudophotosphere on Day 248

To determine the WD temperature on day 248, we assume that both the far-UV fluxes and the supersoft X-ray photons are produced by the long- and short-wavelength parts of the WD radiation. The former is given by the model SED (see Figure 13) and the latter by the supersoft X-ray source as suggested by the low hardness ratio  $F(0.45\text{--}1\text{ keV})/F(0.3\text{--}0.45\text{ keV}) \sim 0.1$  on day 248 (see Figure 1 of Shore et al. 2016) and no X-ray flux detection below  $22\text{ Å}$  during the maximum of the SSS phase (Nelson et al. 2013; Ness et al. 2013). Under this assumption, we can write the ratio

$$\frac{Q^{100}(\text{XRT})}{Q^{248}(\text{XRT})} = \frac{c^{100}(\text{XRT})}{c^{248}(\text{XRT})} = R, \quad (11)$$

where  $Q^{100}(\text{XRT})$  and  $Q^{248}(\text{XRT})$  are photon rates ( $\text{s}^{-1}$ ) emitted by the WD photosphere within the *Swift*-XRT range (0.3–10 keV) attenuated with  $N_{\text{H}}$ , while  $c^{100}(\text{XRT})$  and  $c^{248}(\text{XRT})$  are photon rates directly measured by *Swift*-XRT on days 100 and 248, respectively. According to Equation (11) of Skopal (2001), the flux of quanta  $Q(\text{XRT})$  can be expressed as

$$Q(\text{XRT}) = \frac{L_{\text{WD}}}{\sigma T_{\text{BB}}^4} f^{\text{abs}}(T_{\text{BB}}), \quad (12)$$

where the function

$$f^{\text{abs}}(T_{\text{BB}}) = \frac{\pi}{hc} \int_{\text{XRT}} \lambda B_{\lambda}(T_{\text{BB}}) e^{-\sigma_{\text{X}}(\lambda) N_{\text{H}}} d\lambda \quad (13)$$

represents the flux of photons emitted by a  $1\text{ cm}^2$  area of the WD photosphere within the *Swift*-XRT range, absorbed by hydrogen column density  $N_{\text{H}}$ . Using Equations (12) and (11), the luminosity of the WD on day 248 can be written as

$$L_{\text{WD}}^{248} = \frac{Q^{100}(\text{XRT})}{R} \frac{\sigma (T_{\text{BB}}^{248})^4}{f^{\text{abs}}(T_{\text{BB}}^{248})}, \quad (14)$$

which for  $L_{\text{WD}} = 4\pi d^2 \theta_{\text{WD}}^2 \sigma T_{\text{BB}}^4$  and the scaling factor  $\theta_{\text{WD}}^2 = F_{\text{WD}}(\lambda)/\pi B_{\lambda}(T_{\text{BB}})$  (e.g., Equations (5) and (6) of Skopal 2005) provides the following equation:

$$\frac{q^{100}(\text{XRT})}{R} \frac{\pi B_{\lambda}(T_{\text{BB}}^{248})}{F_{\text{WD}}^{248}(\lambda)} - f^{\text{abs}}(T_{\text{BB}}^{248}) = 0, \quad (15)$$

where  $q^{100}(\text{XRT}) = Q^{100}(\text{XRT})/4\pi d^2$  ( $\text{cm}^{-2}\text{ s}^{-1}$ ). For the parameter  $q^{100}(\text{XRT})$  given by Equation (12),  $R$  derived from observations, and the flux of the WD,  $F_{\text{WD}}^{248}(\lambda)$ , the solution of Equation (15) provides the WD temperature and Equation (14) its luminosity on day 248.

For the measured photon rates  $c^{100}(\text{XRT}) = 35 \pm 5$  and  $c^{248}(\text{XRT}) = 0.025 \pm 0.005\text{ s}^{-1}$  (see Figure 1 of Shore et al. 2016), i.e.,  $R = 1500 \pm 500$ ,  $Q^{100}(\text{XRT}) = 1.1 \times 10^{46}\text{ s}^{-1}$  (for  $L_{\text{WD}}$ ,  $T_{\text{BB}}$ , and  $N_{\text{H}}$  in Table 3), i.e.,  $q^{100}(\text{XRT}) = 4.54\text{ cm}^{-2}\text{ s}^{-1}$  and the WD flux at, e.g.,  $\lambda = 1195\text{ Å}$ ,  $F_{\text{WD}}^{248}(1195) = 1.37 \times 10^{-12}\text{ erg cm}^{-2}\text{ s}^{-1}\text{ Å}^{-1}$ , Equations (15) and (14) yield  $T_{\text{BB}}^{248} = 227 \pm 5\text{ kK}$  and  $L_{\text{WD}}^{248} = (2.3 \pm 0.6) \times 10^{38}\text{ erg s}^{-1}$ , respectively. Figure 13 demonstrates the principle of this approach in a graphical form.



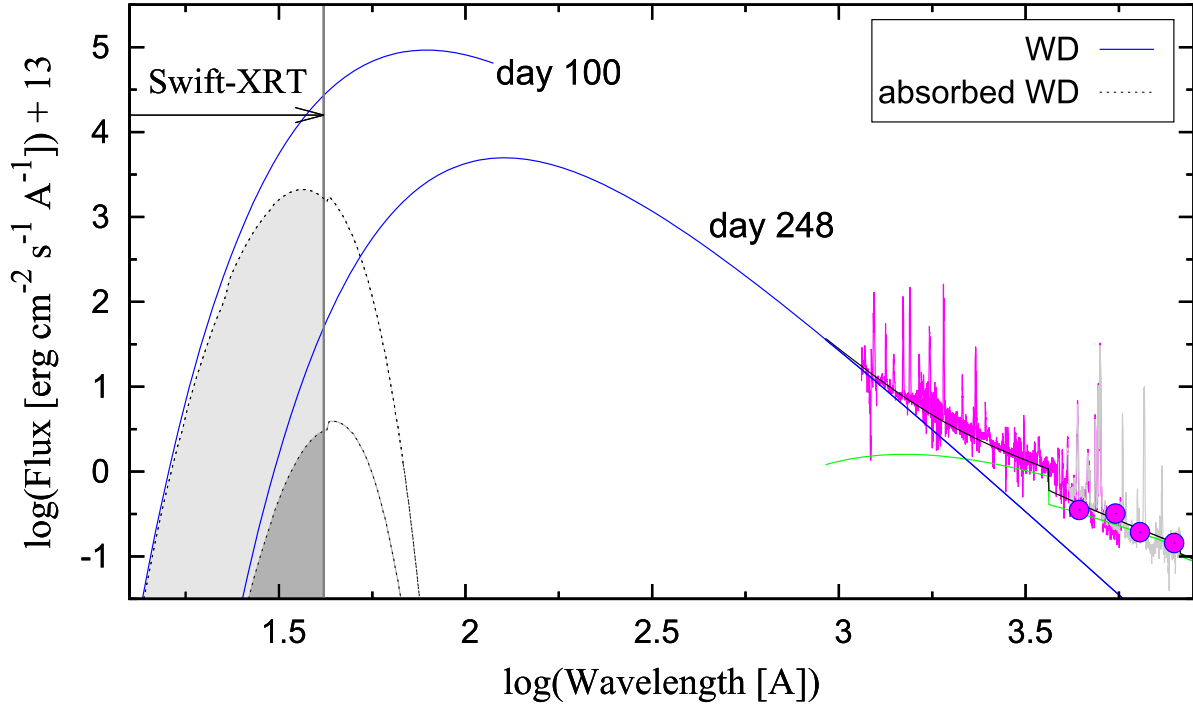


**Figure 13.** On day 248, the WD radiation was determined by scaling its long-wavelength part to dereddened far-UV fluxes and the temperature, at which the radiation produces the X-ray photons rate as measured by *Swift*-XRT (i.e., above 0.3 keV; the gray area). Compared is the absorbed and model WD radiation from day 100 (see text).

## Appendix B

### Dust Emission from a Flat Disk

According to Section 4.2.2, the geometry of emitting dust can be approximated by a flat disk encompassing the central heating source. If the disk is optically thick and radiates locally like a blackbody, the observed flux distribution of the disk,  $F_\lambda$ , at a distance  $d$  is given by contributions from blackbody annuli,  $2\pi r dr$ , integrated through the entire disk, i.e.,

$$F_\lambda = \frac{2\pi \cos(i)}{d^2} \int_{R_{\text{in}}}^{R_{\text{disk}}} B_\lambda(T_{\text{disk}}(r)) r dr, \quad (16)$$

where  $i$  is the angle between the line of sight and the normal to the disk plane,  $R_{\text{disk}}$  its radius, and  $T_{\text{disk}}(r)$  the radial temperature structure of the disk. According to the model SED,  $T_{\text{disk}}(r)$  can be assumed to be constant throughout the dusty disk. Thus, assuming  $T_{\text{disk}}(r) = T_D$  and the inner radius  $R_{\text{in}} \ll R_{\text{disk}}$ , the observed bolometric flux of the disk can be approximated by

$$F_{\text{bol}} = \left(\frac{R_{\text{disk}}}{d}\right)^2 \cos(i) \sigma T_D^4, \quad (17)$$

which gives the disk radius,

$$R_{\text{disk}} = \left(\frac{d^2 F_{\text{bol}}}{\sigma T_D^4 \cos(i)}\right)^{1/2} = R_D^{\text{eff}} / \sqrt{\cos(i)} \quad (18)$$

and the disk luminosity,

$$L_{\text{disk}} = 4\pi d^2 F_{\text{bol}} / \cos(i) = L_D / \cos(i). \quad (19)$$

## ORCID iDs

Augustin Skopal  <https://orcid.org/0000-0002-8312-3326>

## References

- Ackermann, M., Ajello, M., Albert, A., et al. 2014, *Sci*, **345**, 554  
 Ahnen, M. L., Ansoldi, S., Antonelli, L. A., et al. 2015, *A&A*, **582**, A67  
 Anderson, G., Fender, R., Chomiuk, L., & Staley, T. 2013, *ATel*, **5428**  
 Aydi, E., Page, K. L., Kuin, N. P. M., et al. 2018, *MNRAS*, **474**, 2679  
 Beardmore, A. P., Osborne, J. P., & Page, K. L. 2013, *ATel*, **5573**  
 Bessell, M. S. 1979, *PASP*, **91**, 589  
 Bjorkman, J. E., & Cassinelli, J. P. 1993, *ApJ*, **409**, 429  
 Bode, M. F., & Evans, A. 2008, *Classical Novae* (2nd ed.; Cambridge: Cambridge Univ. Press)  
 Brown, R. L., & Mathews, W. G. 1970, *ApJ*, **160**, 939  
 Burlak, M. A., Esipov, V. F., Komissarova, G. V., et al. 2015, *BaltA*, **24**, 109  
 Cardelli, J. A., Clayton, G. C., & Mathis, J. S. 1989, *ApJ*, **345**, 245  
 Cariková, Z., & Skopal, A. 2012, *A&A*, **548**, A21  
 Cheung, C. C., Jean, P., Shore, S. N., et al. 2016, *ApJ*, **826**, 142  
 Chochol, D., Shugarov, S., Katysheva, N., & Volkov, I. 2015, *PoS*, **2015**, 56  
 Chochol, D., Shugarov, S., Pribulla, T., & Volkov, I. 2014, *CoSka*, **43**, 330  
 Chomiuk, L., Linford, J., Finzell, T., et al. 2013, *ATel*, **5382**  
 Chomiuk, L., Linford, J. D., Yang, J., et al. 2014, *Natur*, **514**, 339  
 Cruddace, R., Paresce, F., Bowyer, S., & Lampton, M. 1974, *ApJ*, **187**, 497  
 Deacon, N. R., Hoard, D. W., Magnier, E. A., et al. 2014, *A&A*, **563**, A129  
 Della Valle, M., & Livio, M. 1995, *ApJ*, **452**, 704  
 Denisenko, D., Jacques, C., Pimentel, E., et al. 2013, *IAUC*, **9258**, 2  
 Derdzinski, A. M., Metzge, B. D., & Lazzati, D. 2017, *MNRAS*, **469**, 1314  
 Diplax, A., & Savage, B. D. 1994, *ApJ*, **427**, 274  
 Evans, A., Banerjee, D. P. K., Gehrz, R. D., et al. 2017, *MNRAS*, **466**, 4221  
 Friedjung, M. 1987, *A&A*, **179**, 164  
 Fruchter, A., Krolik, J. H., & Rhoads, J. E. 2001, *ApJ*, **563**, 597  
 Gallagher, J. S., & Starrfield, S. 1978, *ARA&A*, **16**, 171  
 Gattuzz, E., Ness, J.-U., Gorczyca, T. W., et al. 2018, *MNRAS*, **479**, 2457  
 Gehrz, R. D., Evans, A., Helton, L. A., et al. 2015, *ApJ*, **812**, 132  
 Gehrz, R. D., Evans, A., Woodward, C. E., et al. 2018, *ApJ*, **858**, 78  
 Hachisu, I., & Kato, M. 2018, *ApJS*, **237**, 4

- Henden, A. A., & Kaitchuck, R. H. 1982, *Astronomical Photometry* (New York: Van Nostrand-Reinhold), 50
- Kaler, J. B., & Jacoby, G. H. 1989, *ApJ*, **345**, 871
- Kato, M., & Hachisu, I. 1994, *ApJ*, **437**, 802
- Kawakita, H., Shinnaka, Y., Arai, A., Arasaki, T., & Ikeda, Y. 2019, *ApJ*, **872**, 120
- Lanz, T., Telis, G. A., Audard, M., et al. 2005, *ApJ*, **619**, 517
- Li, K.-L., Metzger, B. D., Chomiuk, L., et al. 2017, *NatAs*, **1**, 697
- Livio, M. 1992, *ApJ*, **393**, 516
- Livio, M., Shankar, A., Burkert, A., & Truran, J. W. 1990, *ApJ*, **356**, 250
- Lloyd, H. M., O'Brien, T. J., & Bode, M. F. 1997, *MNRAS*, **284**, 137
- Mason, E., Shore, S. N., De Gennaro Aquino, I., et al. 2018, *ApJ*, **853**, 27
- Munari, U., & Henden, A. 2013, *IBVS*, **6087**, 1
- Munari, U., Henden, A., Dallaporta, S., & Cherini, G. 2013a, *IBVS*, **6080**
- Munari, U., Maitan, A., Moretti, S., & Tomaselli, S. 2015, *NewA*, **40**, 28
- Munari, U., Valisa, P., Milani, A., & Cetrulo, G. 2013b, *ATel*, **5297**
- Mürset, U., & Nussbaumer, H. 1994, *A&A*, **282**, 586
- Nakano, S. 2013, *CBET*, **3628**, 1
- Nelson, T., Mukai, K., Chomiuk, L., & Sokoloski, J. 2013, *ATel*, **5593**
- Ness, J. U., Schwarz, G. J., Page, K. L., et al. 2013, *ATel*, **5626**
- Nussbaumer, H., Schmid, H. M., & Vogel, M. 1989, *A&A*, **211**, L27
- Nussbaumer, H., & Vogel, M. 1987, *A&A*, **182**, 51
- Osborne, J. P., Page, K., Beardmore, A., et al. 2013, *ATel*, **5505**
- Özdönmez, A., Ege, E., Güver, T., & Ak, T. 2018, *MNRAS*, **476**, 4162
- Özdönmez, A., Güver, T., Cabrera-Lavers, A., & Ak, T. 2016, *MNRAS*, **461**, 1177
- Page, K. L., & Beardmore, A. P. 2013, *ATel*, **5429**
- Page, K. L., Osborne, J. P., Kuin, N. P. M., et al. 2013, *ATel*, **5470**
- Prialnik, D., & Kovetz, A. 1995, *ApJ*, **445**, 789
- Schaefer, B. E. 2018, *MNRAS*, **481**, 3033
- Schaefer, G. H., ten Brummelaar, T., Gies, R. D., et al. 2014, *Natur*, **515**, 234
- Schlegel, D. J., Finkbeiner, D. P., & Davis, M. 1998, *ApJ*, **500**, 525
- Schmid, H. M. 1995, *MNRAS*, **275**, 227
- Schwarz, G. J., Hauschildt, P., Starrfield, S., et al. 1998, *MNRAS*, **300**, 931
- Schwarz, G. J., Shore, S. N., Starrfield, S., et al. 2001, *MNRAS*, **320**, 103
- Shafter, A. W., Rau, A., Quimby, R. M., et al. 2009, *ApJ*, **690**, 1148
- Shaviv, N. J. 1998, *ApJL*, **494**, L193
- Shaviv, N. J., & Dotan, C. 2010, *MmSAI*, **81**, 350
- Shaviv, N. J., & Dotan, C. 2012, *MmSAI*, **83**, 792
- Shore, S. N., Kuin, N. P., Mason, E., & De Gennaro Aquino, I. 2018, *A&A*, **619**, A104
- Shore, S. N., Mason, E., Schwarz, G. J., et al. 2016, *A&A*, **590**, A123
- Shore, S. N., Schwarz, G. J., Alton, K., et al. 2013a, *ATel*, **5409**
- Shore, S. N., Schwarz, G. J., Starrfield, S., et al. 2013b, *ATel*, **5624**
- Skopal, A. 2001, *A&A*, **366**, 157
- Skopal, A. 2005, *A&A*, **440**, 995
- Skopal, A. 2007, *NewA*, **12**, 597
- Skopal, A. 2014, in *ASP Conf. Ser.* 490, *Stella Novae: Past and Future Decades*, ed. P. A. Woudt & V. A. R. M. Ribeiro (San Francisco, CA: ASP), **211**
- Skopal, A. 2015a, *NewA*, **36**, 116
- Skopal, A. 2015b, *NewA*, **36**, 128
- Skopal, A. 2015c, *NewA*, **34**, 123
- Skopal, A., Drechsel, D., Tarasova, T., et al. 2014, *A&A*, **569**, A112
- Skopal, A., Pribulla, T., Buil, Ch., Vittone, A. A., & Errico, L. 2008, in *ASP Conf. Ser.* 401, *RS Ophiuchi (2006) and the Recurrent Nova Phenomenon*, ed. A. Evans (San Francisco, CA: ASP), **227**
- Skopal, A., Shugarov, S., Yu., Sekeráš, M., et al. 2017, *A&A*, **604**, A48
- Skopal, A., Tarasova, T. N., Wolf, M., Dubovský, P. A., & Kudzej, I. 2018, *ApJ*, **858**, 120
- Skopal, A., Vittone, A. A., Errico, L., et al. 2006, *A&A*, **453**, 279
- Starrfield, S., Iliadis, Ch., & Hix, W. R. 2008, in *Classical Novae*, ed. M. F. Bode & A. Evans (Cambridge: Cambridge Univ. Press), **77**
- Starrfield, S., Iliadis, Ch., & Hix, W. R. 2016, *PASP*, **128**, 051001
- Taranova, O. G., Tatarnikov, A. M., Shenavrin, V. I., & Tatarnikova, A. A. 2014, *AstL*, **40**, 120
- Tarasova, T. N., & Skopal, A. 2016, *AstL*, **42**, 10
- Wilms, J., Allen, A., & McCray, R. 2000, *ApJ*, **542**, 914
- Yaron, O., Prialnik, D., Shara, M. M., & Kovetz, A. 2005, *ApJ*, **623**, 398